Conditions for traveling waves in spiking neural networks

Johanna Senk[1*], Karolína Korvasová[1], Jannis Schuecker[1], Espen Hagen[1,2], Tom Tetzlaff[1], Markus Diesmann[1,3,4], Moritz Helias[1,4]

1 Institute of Neuroscience and Medicine (INM-6) and Institute for Advanced Simulation (IAS-6) and JARA Institute Brain Structure-Function Relationships (INM-10), Jülich Research Centre, Jülich, Germany
2 Department of Physics, University of Oslo, Oslo, Norway
3 Department of Psychiatry, Psychotherapy and Psychosomatics, Medical Faculty, RWTH Aachen University, Aachen, Germany
4 Department of Physics, Faculty 1, RWTH Aachen University, Aachen, Germany

* j.senk@fz-juelich.de

Abstract

Spatiotemporal patterns such as traveling waves are frequently observed in recordings of neural activity. The mechanisms underlying the generation of such patterns are largely unknown. Previous studies have investigated the existence and uniqueness of different types of waves or bumps of activity using neural-field models, phenomenological coarse-grained descriptions of neural-network dynamics. But it remains unclear how these insights can be transferred to more biologically realistic networks of spiking neurons, where individual neurons fire irregularly. Here, we employ mean-field theory to reduce a microscopic model of leaky integrate-and-fire (LIF) neurons with distance-dependent connectivity to an effective neural-field model. In contrast to existing phenomenological descriptions, the dynamics in this neural-field model depends on the mean and the variance in the synaptic input, both determining the amplitude and the temporal structure of the resulting effective coupling kernel. For the neural-field model we derive conditions for the existence of spatial and temporal oscillations and periodic traveling waves using linear stability analysis. We first prove that periodic traveling waves cannot occur in a single homogeneous population of neurons, irrespective of the form of distance dependence of the connection probability. Compatible with the architecture of cortical neural networks, traveling waves emerge in two-population networks of excitatory and inhibitory neurons as a combination of delay-induced temporal oscillations and spatial oscillations due to distance-dependent connectivity profiles. Finally, we demonstrate quantitative agreement between predictions of the analytically tractable neural-field model and numerical simulations of both networks of nonlinear rate-based units and networks of LIF neurons.

Author summary

Effective coarse-grained models are often developed to capture the dynamics of complex systems composed of large numbers of interacting units. Mapping the microscopic level to simplified coarse-grained equations facilitates analytical predictions of the large-scale dynamics. A prerequisite for this approach is a quantitative relationship between both levels of description. Here, we explore the origin of wave-like phenomena in measured brain activity by deriving such a

relationship between a network of biologically motivated spiking neurons and a neural-field model. Using the neural-field model, we derive conditions for the existence of periodic traveling waves based on the widths of spatial connectivity profiles and transmission delays. The explicit link between the two models delivers a recipe for the construction of spatial connectivity profiles that support traveling waves in networks of spiking neurons with sufficiently large transmission delays.

1 Introduction

Experimental recordings of neural activity frequently reveal spatiotemporal patterns such as traveling waves propagating across the cortical surface [1–8] or within other brain regions such as the thalamus [3, 9] or the hippocampus [10]. These large-scale dynamical phenomena are detected in local-field potentials (LFP) [11] and in the spiking activity [12] recorded with multi-electrode arrays, by voltage-sensitive dye imaging [13], or by two-photon imaging monitoring the intracellular calcium concentration [14]. They have been reported in in-vitro and in in-vivo experiments, in both anesthetized and awake states, and during spontaneous as well as stimulus-evoked activity [3].

Previous modeling studies have shown that networks of spiking neurons with distance-dependent connectivity, extending in one- or two-dimensional space, can exhibit a variety of such spatiotemporal patterns [15–18]. For illustration, consider the example in Fig 1. Depending on the choice of transmission delays, the spatial reach of connections and the strength of inhibition, a network of leaky integrate-and-fire (LIF) model neurons generates asynchronous-irregular activity (A), spatial patterns that are persistent in time (B), spatially uniform temporal oscillations (C), or propagating waves (D). Distance-dependent connectivity is a prominent feature of biological networks. In the neocortex, local connections are established within a radius of about $500\,\mu$m around a neuron's cell body [19], and the probability of two neurons being connected decays with distance [20–22].

So far, the formation of spatiotemporal patterns in neural networks has mainly been studied by means of phenomenological neural-field models describing network dynamics at a macroscopic spatial scale [23–25]. Such models can describe patterns in recorded brain activity that are related to movement [26] or occur in response to a visual stimulus [27]. Neural-field models are formulated with continuous nonlinear integro-differential equations for a spatially and temporally resolved activity variable and usually possess an effective distance-dependent connectivity kernel. These models provide insights into the existence and uniqueness of diverse patterns which are stationary or nonstationary in space and time, such as waves, wave fronts, bumps, pulses, and periodic patterns (reviewed in [28–34]). There are two main techniques for analyzing spatiotemporal patterns in neural-field models [32]: First, in the constructive approach introduced by Amari [25], bump or wave solutions are explicitly constructed by relating the spatial and temporal coordinates of a nonlinear system (reviewed in [28, Section 7] and [32, Sections 3-4]). Second, the emergence of periodic patterns is studied with bifurcation theory as in the seminal works of Ermentrout and Cowan [35–38]. In this latter framework, linear stability analysis is often employed to detect pattern-forming instabilities and to derive conditions for the onset of pattern formation (see for example [39, 40] or the reviews [28, Section 8] and [32, Section 5]). There are four general classes of states that can linearly bifurcate from a homogeneous steady state: a new uniform stationary state, temporal oscillations (spatially uniform and periodic in time, also known as global 'bulk oscillations' [41]), spatial oscillations (spatially periodic and stationary in time), and periodic traveling waves (spatially and temporally periodic), see [28, Section 8] and [42–44]. The analysis of these states is

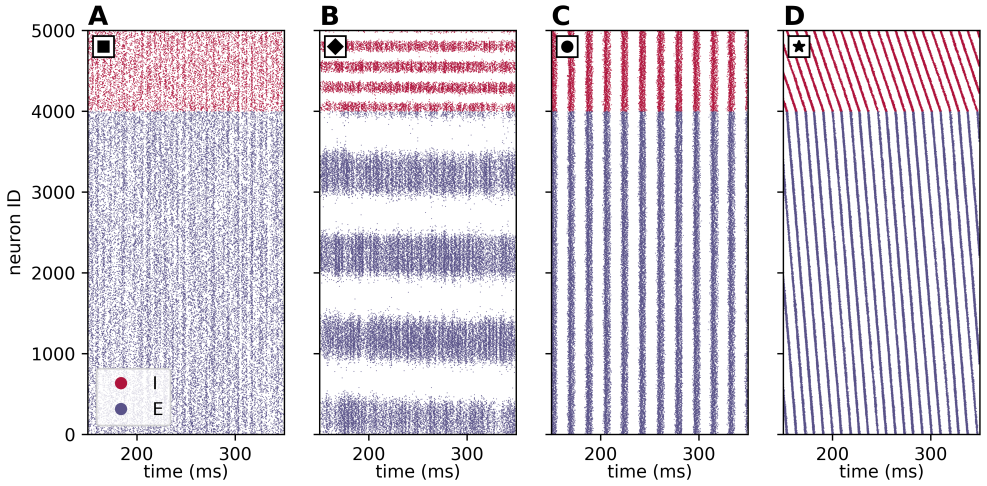

Figure 1. Spatiotemporal patterns in a spiking neural network model. Spiking activity of recurrently connected populations of excitatory (E, blue) and inhibitory (I, red) leaky integrate-and-fire neurons. Each dot represents the spike-emission time of a particular neuron. Neurons within each population are equally spaced on a ring with perimeter of 1 mm. Each neuron receives a fixed number of incoming connections from its excitatory (inhibitory) neighbors uniformly and randomly drawn within a distance of R_E (R_I). The spike-transmission delay d, the widths R_E and R_I of the spatial connectivity profiles, and the relative inhibitory synaptic weight g are varied. **A** Asynchronous-irregular activity ($d = 1\,\mathrm{ms}$, $R_\mathrm{E} = R_\mathrm{I} = 0.4\,\mathrm{mm}$, $g = 6$). **B** Oscillations in space ($d = 3\,\mathrm{ms}$, $R_\mathrm{E} = 0.1\,\mathrm{mm}$, $R_\mathrm{I} = 0.15\,\mathrm{mm}$, $g = 5$). **C** Oscillations in time ($d = 6\,\mathrm{ms}$, $R_\mathrm{E} = R_\mathrm{I} = 0.4\,\mathrm{mm}$, $g = 7$). **D** Propagating waves ($d = 3\,\mathrm{ms}$, $R_\mathrm{E} = 0.2\,\mathrm{mm}$, $R_\mathrm{I} = 0.07\,\mathrm{mm}$, $g = 5$). For remaining parameters, see Fig 12.

often called '(linear) Turing instability analysis' [29, 44, 45] referring to the work of Turing on patterns in reaction-diffusion systems [46]. The respective instabilities leading to these states are termed: a firing rate instability, Hopf instability [47], Turing instability, and Turing-Hopf [42] or 'wave' [40] instability. The instabilities generating temporally periodic patterns (Hopf and Turing-Hopf instabilities) are known as 'dynamic' [44] or 'nonstationary' [48] instabilities, in contrast to 'static' [44] or 'stationary' [48] instabilities generating temporally stationary patterns. The emergence of pattern-forming instabilities has been investigated with respect to system parameters such as the spatial reach of excitation and inhibition in an effective connectivity profile [28]; specifically without transmission delays [49, 50], or with constant [42, 51], distance-dependent [40, 41, 43, 45, 52–56] or both types [57, 58] of delays.

Neural-field models treat neural tissue as a continuous excitable medium and describe neural activity in terms of a space and time dependent real-valued quantity. Throughout the current work the spatial coordinate refers to physical space, although in general it could also be interpreted as feature space. At the microscopic scale, in contrast, neural networks are composed of discrete units (neurons) – which interact via occasional short stereotypical pulses (spikes) rather than continuous quantities like firing rates. In the neocortex, spiking activity is typically highly irregular and sparse [59, 60], with weak pairwise correlations [61]. To date, a rigorous link between this microscopic level and the macroscopic description by neural-field models is lacking [31, 33, 62, 63]. While randomly connected spiking networks have been

extensively analyzed using mean-field approaches [60, 64–66], the theoretical understanding of spatially structured spiking networks is still deficient. Hence, it remains unclear how to qualitatively transfer insights on the formation of spatiotemporal patterns from neural fields to networks of spiking neurons. Moreover, it is unknown how the multitude of neuron, synapse and connectivity parameters of spiking neural networks relates to the effective parameters in neural-field models. A quantitative link between the two levels of description is, for example, required for adjusting parameters in a network of spiking neurons such that it generates a specific type of spatiotemporal pattern, and to enable model validation by comparison with experimental data.

Different efforts have already been undertaken to match spiking and time-continuous rate models with spatial structure. Certain assumptions and approximations allow the application of techniques for analyzing spatiotemporal patterns developed for neural-field models. The above mentioned constructive approach [25], for example, can be applied to networks of spiking neurons under the assumption that every neuron spikes at most once, thus ignoring the sustained spike generation and after-spike dynamics of biological neurons [67–69]. A related simplification substitutes a spike train by an ansatz for a wave front. This leads to a mean-field description of single-spike activity often applied to a spike-response model [70–73]. Traveling-wave solutions have also been proposed for a network of coupled oscillators and a corresponding continuum model [74]. In the framework of bifurcation theory, Roxin et al. [42, 51] demonstrate a qualitative agreement between a neural-field model and a numerically simulated network of Hodgkin-Huxley-type neurons in terms of emerging spatiotemporal patterns. However, the authors do not observe stable traveling waves in the spiking network, even though the neural-field model predicts their occurrence. In the limit of slow synaptic interactions, spiking dynamics can be reduced to a mean-firing-rate model for studying bifurcations [75–77]. An example is the lighthouse model [78, 79], defined as a hybrid between a phase oscillator and a firing-rate model, that reduces to a pure rate model for slow synapses [80]. Laing and Chow [81] demonstrate a bump solution in a spiking network and discuss a corresponding rate model. Recently, the group around Doiron and Rosenbaum explored in a sequence of studies spatially structured networks of LIF neurons without transmission delays in the continuum limit with respect to the spatial widths of connectivity. The authors focus on the existence of the balanced state [82], the structure of correlations in the spiking activity [83], and bifurcations in the linearized dynamics in relation to network computations [84]. Kriener et al. [85] employ static mean-field theory and extend the linearization of a network of LIF neurons with constant delays as described by Brunel [65], to spatially structured networks. The work derives conditions for the appearance of spontaneous symmetry breaking that leads to stationary periodic bump solutions (spatial oscillations), and distinguish between the mean-driven and the fluctuation driven regime.

Despite these previous works on spatially structured network models of spiking neurons and attempts to link them with neural-field models, there still exists no systematic way of mapping parameters between these models. Furthermore, none of these studies focuses on uncovering the underlying mechanism of periodic traveling waves in spiking networks. In the present work we establish the so far missing, quantitative link between a sparsely connected network of spiking LIF neurons with spatial structure and a typical neural-field model. An explicit parameter mapping between the two levels of description allows us to study the origin of spatiotemporal patterns analytically in the neural-field model using linear stability analysis, and to reproduce the predicted patterns in spiking activity. We employ mean-field theory to derive the neural-field model as an effective rate model depending on the dynamical

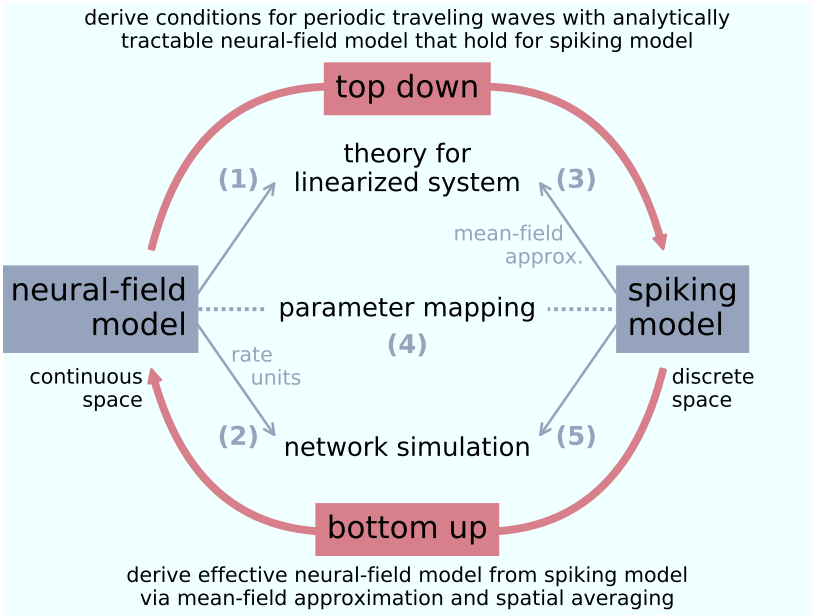

Figure 2. Mapping microscopic single-neuron dynamics to spatially averaged population dynamics. **(1)** Conditions for periodic traveling waves in a neural-field model. **(2)** Network simulation of discrete nonlinear rate neurons. **(3)** Mean-field approximation of the spiking model and spatial averaging lead to an effective linearized continuous system. **(4)** Parameter mapping between spiking and neural-field model. **(5)** Network simulation of spiking neurons and validation of analytical results.

working point of the network that is characterized by both the mean and the variance of the synaptic input. The rate model accounts for biological constraints such as a static weight that is either positive (excitatory) or negative (inhibitory) and a spatial profile that can be interpreted as a distance-dependent connection probability. Given these constraints, we show that periodic traveling waves cannot occur in a single homogeneous population irrespective of the shape of distance-dependent connection probability. For two-population networks of excitatory and inhibitory neurons, in contrast, traveling waves emerge for specific types of spatial profiles and for sufficiently large delays, as shown in Fig 1D.

The remainder of the study is structured as follows: In Results we derive the conditions for the existence of periodic traveling waves for a typical neural-field model by linear stability analysis, present an effective model corresponding to the microscopic description of spiking neurons, compare the two models, and show simulation results for validation. In Discussion we put our results in the context of previous literature. Finally, Methods contains details on our approach. An account of the presented work has previously been published in abstract form in [86].

2 Results

We aim to establish a mapping between two different levels of description for spatially structured neural systems to which we refer as ‘neural-field model’ and ‘spiking model’ based on the initial model assumptions. While the neural-field model describes neural activity as a quantity that is continuous in space and time, the spiking model assumes a network of recurrently connected spiking model neurons in discrete space. Our

methodological approach for mapping between these two models, as well as the structure of this Section, are illustrated in Fig 2. (1) We start in Sections 2.1-2.3 with linear stability analysis of a typical neural-field model that is a well-known and analytically tractable rate equation. This approach builds on existing literature (cf. [28, Section 8] and [32, Section 5]) and introduces the concepts of our study with modest mathematical efforts. We analyze the neural-field model for one and two populations and derive conditions for the occurrence of periodic traveling waves based on spatial connectivity profiles and transmission delays. (2) In Section 2.4 we continue with simulations of a discrete version of the neural-field model, a network of nonlinear rate-based units, and show that the results from our linear analysis indeed accurately predict transitions between network states (homogeneously steady, spatial oscillations, temporal oscillations, waves). (3) Then, in Section 2.5 we linearize the population dynamics of networks of discrete spiking leaky integrate-and-fire (LIF) neurons using mean-field theory and derive expressions similar to the neural-field model. (4) Thus, both the linearized neural-field and spiking models can be treated in a conceptually similar manner, with the exception of an effective coupling kernel which is mathematically more involved for the spiking model. In Section 2.6 we perform a parameter mapping between the biophysically motivated parameters of the spiking model and the effective parameters of a neural-field model. (5) Finally, in Section 2.7 we demonstrate that the insights obtained in the analysis of the neural-field model apply to networks of simulated LIF neurons: The bifurcations indeed appear at the theoretically predicted parameter values.

In summary, the mapping of a microscopic spiking network model to a continuum neural-field model (bottom up) allows us to transfer analytically derived insights from the neural-field model directly to the spiking model (top down).

2.1 Linear stability analysis of a neural-field model

We first consider a neural-field model with a single population defined as a continuous excitable medium with a translation-invariant interaction kernel and delayed interaction in one spatial dimension. The dynamics follows an integro-differential equation

$$\tau \frac{\mathrm{d}u}{\mathrm{d}t}(x,t) + u(x,t) = \int_{-\infty}^{\infty} P(x-y)\ \psi(u(y,t-d))\ \mathrm{d}y. \tag{1}$$

The variable u describes the activity of the neural population at position x at time t. Here $\tau > 0$ denotes a time constant and $d > 0$ a transmission delay. The function ψ describes the nonlinear transformation of the output activity u if considered as input to the neural field. The function P specifies the translation-invariant connectivity depending only on the displacement $r = x - y$ where x and y denote neuron positions. Earlier studies show that specific choices for connectivities P and nonlinear transformations ψ result in spatiotemporal patterns such as waves or bumps [28–34].

Here, we assume that the connectivity P is isotropic and define $P(r) := w\,p(r)$. The scalar weight w can either be positive (excitatory) or negative (inhibitory). The spatial profile $p(r)$ is a symmetric probability density function with the properties $p(r) = p(-r)$, $p(r) > 0$ for $r \in (-\infty, \infty)$ and $\int_{-\infty}^{\infty} p(r)\ \mathrm{d}r = 1$. Fig 3A shows, as an example, a boxcar-shaped spatial profile with width R, defined by $p(r) = \frac{1}{2R}\Theta(R - |r|)$ where Θ denotes the Heaviside function.

Throughout this study we investigate bifurcations of the system Eq 1 between a state of spatially and temporally homogeneous activity $u(x,t) = u_0$ to states where the activity shows structure in the temporal domain, in the spatial domain, or both. For this purpose we use Turing instability analysis [29, 39, 40]. Initially we assume that the

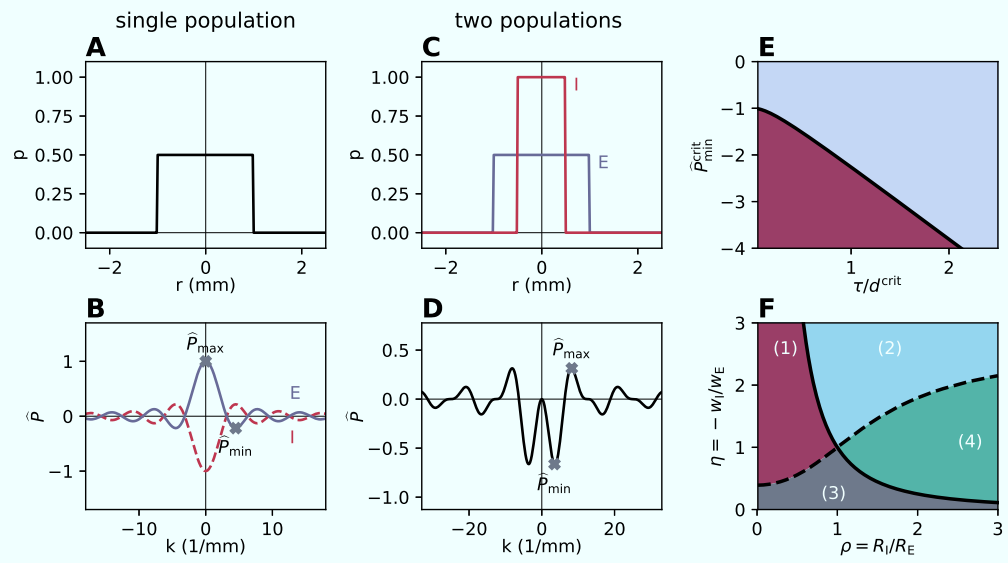

Figure 3. Effective profile yields conditions for traveling waves.
A Boxcar-shaped spatial profile p of width $R = 1\,\mathrm{mm}$ for a single population. **B** Effective profile $\widehat{P}$ (blue curve) denotes Fourier transform of spatial profile $\widehat{p}$ times positive weight $w_\mathrm{E} = 1$. Gray crosses indicate maximum $\widehat{\mathrm{P}}_\mathrm{max}$ and minimum $\widehat{P}_\mathrm{min}$. Same spatial profile but with negative weight ($w_\mathrm{I} = -w_\mathrm{E}$) yields mirrored curve (red, dashed line). **C** Spatial profiles of different widths for two populations E ($R_\mathrm{E} = 1\,\mathrm{mm}$, blue) and I ($R_\mathrm{I} = 0.5\,\mathrm{mm}$, red). **D** Effective profile: $\widehat{P}\,(k) = w_\mathrm{E}\widehat{p}_\mathrm{E}\,(k) + w_\mathrm{I}\widehat{p}_\mathrm{I}\,(k)$. **E** Transition curve $\widehat{P}^\mathrm{crit}_\mathrm{min}(\tau/d^\mathrm{crit})$ given by Eq 10 for Hopf bifurcation indicating onset of delay-induced oscillations (appearing in purple region) with time constant τ and delay d. **F** Transition curves for relative width $\rho = R_\mathrm{I}/R_\mathrm{E}$ and relative weight $\eta = -w_\mathrm{I}/w_\mathrm{E}$. Colored regions indicate which extremum, the minimum $\widehat{P}_\mathrm{min}$ or the maximum $\widehat{P}_\mathrm{max}$, has larger absolute value and if the dominant one occurs at $k = 0$ or at $k > 0$. (1, purple): $\widehat{P}_\mathrm{min}$ appears at $k_\mathrm{min} > 0$. (2, light blue): $\widehat{P}_\mathrm{min}$ appears at $k_\mathrm{min} = 0$. (3, dark gray): $\widehat{P}_\mathrm{max}$ appears at $k_\mathrm{max} = 0$. (4, green) $\widehat{P}_\mathrm{max}$ appears at $k_\mathrm{max} > 0$.

model parameters are chosen such that the homogeneous solution is locally asymptotically stable, implying that small perturbations away from u_0 will relax back to this baseline. We ask the question: In which regions of the parameter space (R, d, w, ψ) is the stability of the homogeneous solution lost? To this end we linearize around the steady state and denote deviations $\delta u(t) = u(t) - u_0$. Without loss of generality we assume the slope $\psi'(u_0)$ of the gain function to be unity; a non-zero slope can be absorbed into a redefinition of w. Because the resulting system is linear and invariant with respect to translations in time and space, its eigenmodes are Fourier-Laplace modes of the form

$$\delta u\,(x,t) = \mathrm{e}^{\mathrm{i}kx}\mathrm{e}^{\lambda t}, \tag{2}$$

where the wave number $k \in \mathbb{R}$ is real and the temporal eigenvalue $\lambda \in \mathbb{C}$ is complex. Solutions constructed from these eigenmodes can oscillate in time and space, and exponentially grow or decay in time. The characteristic equation (see Eq 31 in Methods)

$$(1+\tau\lambda)\ \mathrm{e}^{\lambda d} = \widehat{P}\,(k)\,, \tag{3}$$

comprises the effective profile $\widehat{P}\,(k) \coloneqq w\widehat{p}\,(k)$. The Fourier transform of the spatial profile is denoted by $\widehat{p}\,(k)$ which, by its definition as a probability density, is maximal at $k=0$ with $\widehat{p}\,(0)=1$ (see Eqs 38 and 39 in Methods). The effective profile for the boxcar-shaped spatial profile is shown in Fig 3B, for excitatory and inhibitory weights with absolute magnitudes of unity.

We next extend the system to two populations, an excitatory one denoted by E, and an inhibitory one by I. Time constants τ and delays d are assumed to be equal for both populations, but u becomes a vector, $u = (u_\mathrm{E}, u_\mathrm{I})^T$, and the connectivity $P\,(r)$ a matrix

$$P\,(r) = \begin{pmatrix} w_\mathrm{EE}\,p_\mathrm{EE}\,(r) & w_\mathrm{EI}\,p_\mathrm{EI}\,(r) \\ w_\mathrm{IE}\,p_\mathrm{IE}\,(r) & w_\mathrm{II}\,p_\mathrm{II}\,(r) \end{pmatrix}. \tag{4}$$

The linearized system again possesses the same symmetries as the counterpart for a single population so that the eigenmodes for the deviation from the stationary state are of the form $\delta u\,(x,t) = v e^{\mathrm{i}kx}\mathrm{e}^{\lambda \mathrm{t}}$ with v denoting a constant vector. Hence, we arrive at an auxiliary eigenvalue problem (see Eq 32 in Methods) with the two eigenvalues

$$\widehat{P}_{1,2}\,(k) = \frac{1}{2}\left(w_\mathrm{EE}\,\widehat{p}_\mathrm{EE}\,(k) + w_\mathrm{II}\,\widehat{p}_\mathrm{II}\,(k) \pm \sqrt{D}\right), \tag{5}$$

where

$$\begin{aligned} D = &\left(w_\mathrm{EE}\,\widehat{p}_\mathrm{EE}\,(k) + w_\mathrm{II}\,\widehat{p}_\mathrm{II}\,(k)\right)^2 \\ &- 4\left(w_\mathrm{EE}\,\widehat{p}_\mathrm{EE}\,(k)\ w_\mathrm{II}\,\widehat{p}_\mathrm{II}\,(k) - w_\mathrm{EI}\,\widehat{p}_\mathrm{EI}\,(k)\ w_\mathrm{IE}\,\widehat{p}_\mathrm{IE}\,(k)\right). \end{aligned} \tag{6}$$

These two eigenvalues play the same role as the effective profile $\widehat{P}$ in the one-population case above. As a consequence, the same characteristic equation Eq 3 holds for both the one- and the two-population system.

In the following example we restrict the weights and the spatial profiles to be uniquely determined by the source population alone, denoted by $w_{\alpha\mathrm{E}} =: w_\mathrm{E}$, $w_{\alpha\mathrm{I}} =: w_\mathrm{I}$ for $\alpha \in \{\mathrm{E}, \mathrm{I}\}$. An illustration of the two spatial profiles of different widths R_E and R_I is shown in Fig 3C. The respective effective profile Eq 5 reducing to $\widehat{P}\,(k) = w_\mathrm{E}\widehat{p}_\mathrm{E}\,(k) + w_\mathrm{I}\widehat{p}_\mathrm{I}\,(k)$ is shown in Fig 3D.

The characteristic equation Eq 3 can be solved for the eigenvalues λ by using the Lambert W function defined as $z = W\,(z)\,\mathrm{e}^{W(z)}$ for $z \in \mathbb{C}$ [87]. The Lambert W function has infinitely many branches, indexed by b, and the branch with the largest real part is denoted the principle branch ($b=0$), see Eqs 35-36 in Methods for a proof. The characteristic equation determines the temporal eigenvalues (see Eq 37 in Methods and compare with [58])

$$\lambda_b(k) = -\frac{1}{\tau} + \frac{1}{d}\,W_b\left(\widehat{P}\,(k)\,\frac{d}{\tau}\mathrm{e}^{\frac{d}{\tau}}\right). \tag{7}$$

2.2 Conditions for spatial and temporal oscillations, and traveling waves

The homogeneous (steady) state of our system is locally asymptotically stable if the real parts of all eigenvalues λ_b are negative

$$\mathrm{Re}\left[W_b\left(\widehat{P}\,(k)\,\frac{d}{\tau}\mathrm{e}^{\frac{d}{\tau}}\right)\right] < \frac{d}{\tau}, \tag{8}$$

for all branches b of the Lambert W function. The system loses stability when the real part of the eigenvalue λ_0 on the principle branch becomes positive at a certain $k = k^*$. Such instabilities may occur either for a positive or a negative argument of the Lambert W function.

We denote the maximum of $\widehat{P}$ as $\widehat{P}_{\max}$ and the minimum as $\widehat{\mathrm{P}}_{\min}$ occurring at $k_{\max}$ and $k_{\min}$, respectively, as indicated in Fig 3B and D. The system becomes unstable for a positive argument of W if $\widehat{P}_{\max} = 1$ where $\mathrm{Re}\left[W_0\left(\frac{d}{\tau}\mathrm{e}^{\frac{d}{\tau}}\right)\right] = \frac{d}{\tau}$ by the definition of the Lambert W function; so equality holds in Eq 8 independent of the values d and τ. The imaginary part of λ_0 is zero at such a transition. If the instability appears at a wave number $k^* = 0$, the population activity is collectively destabilized. This transition corresponds in networks of binary neurons and of spiking neurons to the transition between the asynchronous irregular (AI) state and the synchronous regular (SR) state, where the system ceases to be stabilized by negative feedback and leaves the balanced state [65, 88]. If this transition appears at a wave number $k^* > 0$, it follows from Eq 2 that the activity shows spatial oscillations that grow exponentially in time.

For a negative argument of W of less than $-1/e$, the eigenvalues Eq 7 come in complex conjugate pairs. The real part of λ_0 becomes positive if the condition

$$\mathrm{Re}\left[W_0\left(\widehat{P}_{\min}\frac{d}{\tau}\mathrm{e}^{\frac{d}{\tau}}\right)\right] = \frac{d}{\tau} \tag{9}$$

is fulfilled with a negative $\widehat{P}_{\min} < -1$. Because the eigenvalues have non-zero imaginary parts, this transition corresponds to a Hopf bifurcation and the onset of temporal oscillations. The condition for this bifurcation has been derived earlier [89, Eq 10]

$$\frac{d^{\mathrm{crit}}}{\tau} = \frac{\pi - \arctan\left(\sqrt{\widehat{P}_{\min}^{\mathrm{crit}^2} - 1}\right)}{\sqrt{\widehat{P}_{\min}^{\mathrm{crit}^2} - 1}}. \tag{10}$$

Here, d^{crit} denotes the critical delay and $\widehat{P}_{\min}^{\mathrm{crit}}$ a critical minimum of the effective profile for points on the transition curve. The system is stable for $\widehat{P}_{\min} > -1$ for all delays. For larger absolute values of $\widehat{P}_{\min}$, the bifurcation point is given by the critical value of the ratio between the time constant and the delay, shown in Fig 3E. If the transition occurs at $k^* = 0$, temporal oscillations emerge in which all neurons of the population oscillate in phase ('bulk oscillations' [41]). In spiking networks this Hopf bifurcation corresponds to the transition from the AI regime to the state termed 'synchronous irregular fast (SI fast)' [60]. If the transition appears for $k^* > 0$, spatial and temporal oscillations occur simultaneously. This phenomenon is known as 'periodic traveling waves', see [28, Section 8] and [42–44]. For the case that the system becomes unstable due to $\widehat{P}_{\max}$ reaching unity, the transition curve in Fig 3E also provides a lower bound $\widehat{P}_{\min}^{\mathrm{crit}}(\tau/d^{\mathrm{crit}})$ above which temporal oscillations do not occur prior to the transition due to $\widehat{P}_{\max}$.

In summary, the system is stable if $\widehat{P}_{\max} < 1$ and $\widehat{P}_{\min} > \widehat{P}_{\min}^{\mathrm{crit}}(\tau/d^{\mathrm{crit}})$. For transitions occurring at either $\widehat{P}_{\max} = 1$ or $\widehat{P}_{\min} = \widehat{P}_{\min}^{\mathrm{crit}}(\tau/d^{\mathrm{crit}})$ we distinguish between solutions with $k^* = 0$ or $k^* > 0$. In Fig 4 we provide an overview of the conditions for bifurcations leading to spatial, temporal, or spatiotemporal oscillatory states. These conditions imply that a one-population neural-field model does not permit traveling waves, which follows from the fact that the absolute value of $\widehat{p}$ is strictly maximal at $k = 0$ (see Eqs 38-39 in Methods). For a purely excitatory population ($w > 0$) the critical minimum $\widehat{P}_{\min}^{\mathrm{crit}}(\tau/d^{\mathrm{crit}})$ therefore cannot be reached

	homogeneous	spatial oscillations	temporal oscillations	traveling waves
$\widehat{P}_{\max}$	< 1	1	< 1	< 1
$\widehat{P}_{\min}$	$> \widehat{P}_{\min}^{\text{crit}}$	$> \widehat{P}_{\min}^{\text{crit}}$	$\widehat{P}_{\min}^{\text{crit}}$	$\widehat{P}_{\min}^{\text{crit}}$
d	$< d^{\text{crit}}$	$< d^{\text{crit}}$	d^{crit}	d^{crit}
k^*	-	> 0	0	> 0

Figure 4. Conditions for the onset of spatial and temporal oscillations, and traveling waves. Gray cells in each column indicate the conditions required for the instability causing the bifurcation. White cells denote the conditions for the respective other bifurcation not to occur. Last row indicates whether the bifurcation happens for zero or nonzero wave number k^*. Here d^{crit} and $\widehat{P}_{\min}^{\text{crit}}$, as defined in Eq 10 and shown in Fig 3E, denote the critical delay and the minimum of the effective profile on the transition curve for a Hopf bifurcation.

while keeping the maximum $\widehat{P}_{\max}$ stable as $\widehat{P}_{\max} > \left|\widehat{P}_{\min}\right|$. For a purely inhibitory population ($w < 0$), the condition $k_{\min} > 0$ is not fulfilled because $\widehat{P}_{\min}$ occurs at $k = 0$ as $\widehat{p}$ has its global maximum at the origin.

For a neural-field model accounting for both excitation and inhibition, however, we can select shapes and parameters of the spatial profiles, weights and the delay that fulfill the conditions for the onset of traveling waves as demonstrated by example in the next section.

2.3 Application to a network with excitation and inhibition

Based on the conditions derived in the previous section, the minimal network in which traveling waves can occur consists of one excitatory (E) and one inhibitory (I) population. As in the example in Section 2.1, we assume that the connection weights and widths of boxcar-shaped spatial profiles only depend on the source population. The effective profile Eq 5 in this case is

$$\widehat{P}(k) = w_{\text{E}} \frac{\sin(R_{\text{E}}k)}{R_{\text{E}}k} + w_{\text{I}} \frac{\sin(R_{\text{I}}k)}{R_{\text{I}}k}, \tag{11}$$

and positive and negative peaks of the profile are responsible for bifurcations to spatial or temporal oscillations or wave solutions, respectively. The previous section derives that in particular the position and height of the minima and maxima of the effective profile are decisive. To assess parameter ranges in which the peaks of the effective profile Eq 11 change qualitatively, we introduce the relative width $\rho := R_{\text{I}}/R_{\text{E}} > 0$ and the relative weight $\eta := -w_{\text{I}}/w_{\text{E}} > 0$, divide $\widehat{P}(k)$ by w_{E} and introduce the rescaled wave number $\kappa = R_{\text{E}}k$ to arrive at the dimensionless reduced profile

$$\widehat{B}(\kappa) = \frac{\sin(\kappa)}{\kappa} - \eta \frac{\sin(\rho\kappa)}{\rho\kappa}, \tag{12}$$

which simplifies the following analysis.

Our aim is to divide the parameter space (ρ, η) into regions that have qualitatively similar shapes of the effective profile. The Methods section describes the derivation of transition curves and Fig 3F illustrates the resulting parameter space. Above the first transition curve $\eta_{t1}(\rho)$ (dashed curve, see Eq 46 in Methods), the absolute value of $\widehat{B}_{\min}$ is larger than $\widehat{B}_{\max}$ (regions 1 and 2), and vice versa below this curve (regions 3 and 4). The second transition curve $\eta_{t2}(\rho)$ (solid curve, see Eq 49 in Methods) indicates whether the extremum with the largest absolute value occurs at $k = 0$

(regions 2 and 3) or at $k > 0$ (regions 1 and 4). The diagram provides the necessary conditions and corresponding parameter combinations required for both spatial and spatiotemporal patterns, purely based on the relative weights and the relative widths which determine the effective profile. The analysis shows that traveling waves require wider excitation than inhibition, $\rho < 1$, because only this relation simultaneously realizes a minimum at a non-zero wave number k^* and a maximum with a peak below unity (see Fig 4).

A neural-field model exhibiting traveling waves can therefore be constructed at will by first selecting a point within region 1 of Fig 3F where $\rho < 1$ and η ensures that $\left|\widehat{B}_{\min}\right| > \widehat{B}_{\max}$. Next, $\widehat{P}$ is fixed by scaling $\widehat{B}$ with the absolute weight w_{E} such that $\widehat{P}_{\max} < 1$ for a stable bump solution and $\widehat{P}_{\min} < -1$ for a Hopf bifurcation. Finally a delay $d > d^{\mathrm{crit}}$ specifies a point below the bifurcation curve shown in Fig 3E, given by the sufficient condition for the Hopf bifurcation in Eq 10. Likewise, solutions for purely temporal oscillations appear in region 2, where $\widehat{P}_{\min} \leq -1$ is attained at a vanishing wave number k and a delay $d > d^{\mathrm{crit}}$; in addition $\widehat{P}_{\max} < 1$ ensures absence of the other bifurcation into spatial oscillations. For purely spatial oscillations, however, the comparison of the absolute values of $\widehat{B}_{\min}$ and $\widehat{B}_{\max}$ is not sufficient; it is hence not sufficient to rely on the dashed curve separating regions 2 and 4 in Fig 3F. A loss of stability due to $\widehat{P}_{\max} > 1$ can emerge not only in region 4 but also in region 2, because even if $\left|\widehat{P}_{\min}\right| > \widehat{P}_{\max}$, stability of $\widehat{P}_{\min}$ can be ensured by a sufficiently short delay $d < d^{\mathrm{crit}}$, as shown in Fig 4.

2.4 Network simulation with nonlinear rate neurons

We have so far only investigated the properties of an analytically tractable linear system that assumes time and space to be continuous variables. Next, we test the derived conditions for the onset of oscillations, summarized in Fig 4, for a nonlinear, discrete system in the continuum limit. We here consider a network of $N_{\mathrm{E}} = 4,000$ excitatory (E) and $N_{\mathrm{I}} = 1,000$ inhibitory (I) rate neurons described by a discrete version of the neural-field equation Eq 1 (see Fig 11 for details). The model neurons within each population are equally spaced on a ring of perimeter $L = 1\,\mathrm{mm}$. This rate-neuron network constitutes an intermediate step towards a network of spiking neurons. Each neuron has a fixed in-degree K_X (fixed number of incoming connections) per source population $X \in \{\mathrm{E}, \mathrm{I}\}$ with connections selected randomly within a distance R_X. A normalization of weights with the in-degree, $w'_X = w_X/K_X$, allows us to interpret p as a connection probability. The time constant τ and the delay d are the same as in the neural-field model. As nonlinear gain function in Eq 1 we choose $\psi(u) = \tanh(u)$.

The neuron activity of four rate-network simulations with different parameter combinations are shown in Fig 5A-D. The location of the specific parameter combinations is illustrated in Fig 5E-G with corresponding markers in the phase diagrams that visualize the stability conditions shown in Fig 3 derived with the neural-field model. Periodic traveling waves are possible if parameters are in the purple regions of the diagrams.

The system simulated in Fig 5A is stable according to the corresponding conditions. The square marker in the lower panels shows that $\widehat{P}_{\max} < 1$ (panel E), and although $\widehat{P}_{\min} < -1$, the delay is small such that the system is far away from the bifurcation (panel F). Indeed, the activity appears to not exhibit any spatial or temporal structure.

Fig 5B illustrates a case where $\widehat{P}_{\max} > 1$ causes an instability (diamond marker in panel E). The Hopf bifurcation is remote in the parameter space (panel F) and panel G ensures $k_{\max} > 0$. A simulation of the corresponding rate-model network again

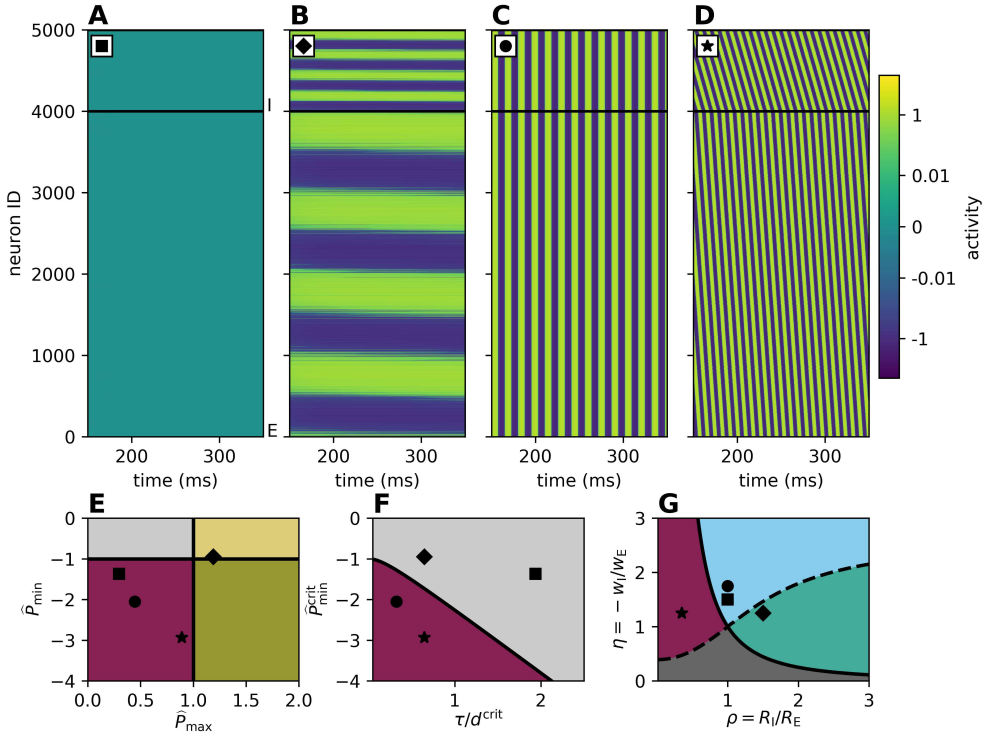

Figure 5. Predictions from linear stability analysis lead to spatiotemporal patterns in simulated network of nonlinear rate neurons. Different parameter combinations, selected according to stability conditions in Fig 4, cause pattern formation in rate-neuron network with tanh gain function. **A-D** Color-coded activity per neuron over time. Neurons within each population are consecutively numbered with a 'neuron ID' according to their position on the ring, and neuron IDs of inhibitory neurons follow the ones of excitatory neurons. **E-F** Phase diagrams showing conditions and parameter choices indicated by corresponding markers. Purple regions indicate the possibility for periodic traveling waves. **A** Stable activity (square marker). **B** Spatial oscillations (diamond marker). **C** Temporal oscillations (circular marker). **D** Periodic traveling waves (star marker). Parameters: d, R_E and R_I as in Fig 1A-D, $w_E = 2.73$ in all panels. **A** $w_I = -4.10$. **B** $w_I = -3.42$. **C** $w_I = -4.79$. **D** $w_I = -3.42$.

confirms the predictions and exhibits stationary spatial oscillations (or periodic bumps) with a wave number of $k_{\max}$. In this finite-sized system with periodic boundary conditions, the bumps are homogeneously distributed across the domain and the wave numbers are integers.

Fig 5C demonstrates temporal oscillations at the parameter combination indicated by the circular marker. We here choose $\widehat{P}_{\max} < 1$ and $\widehat{P}_{\min} < -1$ (panel E). The latter condition leads to an entire range of delays that are beyond the bifurcation in panel F; we choose a delay slightly larger than the critical delay, lying to the left of the bifurcation curve. Inferred from panel G, $k_{\min} = 0$ and, as expected from the analytical prediction, the oscillations observed in simulations of the rate-neuron network are purely temporal.

Finally, Fig 5D depicts periodic traveling waves (denoted by star marker), as predicted by the analytically tractable neural-field model. The instability results from $\widehat{P}_{\min} < \widehat{P}^{\text{crit}}_{\min}$ (panel F) and occurs at $k_{\min} > 0$ (panel G) while $\widehat{P}_{\max}$ remains stable (panel E).

2.5 Linearization of spiking network model

To assess the validity of the predictions obtained from the analytical model for biologically more realistic spiking-neuron networks, we next linearize the dynamics of spiking leaky integrate-and-fire (LIF) neurons and derive a linear system similar to the neural-field model above. The sub-threshold dynamics of a single LIF neuron i with exponentially decaying synaptic currents is described by a set of differential equations for the time evolution of the membrane potential V_i and its synaptic current I_i as

$$\begin{aligned} \tau_\mathrm{m}\frac{dV_i}{dt} &= -V_i + I_i\left(t\right), \\ \tau_\mathrm{s}\frac{dI_i}{dt} &= -I_i + \tau_\mathrm{m}\sum_j J_{ij}s_j\left(t-d\right), \end{aligned} \tag{13}$$

where we follow the convention of [90] (see Eq 60 in Methods for the relation to physical units). This definition, with both quantities V_i and I_i having the same unit, conserves the total integrated charge per impulse flowing into the membrane independent of the choice of the synaptic time constant τ_s. The membrane time constant, defined as $\tau_\mathrm{m} = R_\mathrm{m}C_\mathrm{m}$ with membrane resistance R_m and membrane capacitance C_m, couples current to the capacitance. We here assume τ_s to be much smaller than τ_m. The term $s_j\left(t\right) = \sum_k \delta\left(t - t_k^j\right)$ denotes a spike train of neuron j which is connected to neuron i with a constant connection strength J_{ij} and transmission delay d. Whenever V_i reaches the threshold V_θ, a spike is emitted and the membrane potential is reset to the resting potential V_r and voltage-clamped for the refractory period τ_ref.

Assuming that a neuron receives many uncorrelated and Poisson-distributed input spikes, and that amplitudes of postsynaptic potentials are small, we apply the diffusion approximation [64, 91, 92] and approximate the input to the neuron by a current with mean μ_i and variance σ_i as given by

$$\tau_\mathrm{m}\sum_j J_{ij}s_j\left(t-d\right) \approx \mu_i\left(t\right) + \sqrt{\tau_\mathrm{m}}\sigma_i\left(t\right)\xi\left(t\right). \tag{14}$$

The term $\xi\left(t\right)$ denotes a Gaussian white noise characterized by $\langle\xi\left(t\right)\rangle = 0$ and $\langle\xi\left(t\right)\xi\left(t'\right)\rangle = \delta\left(t-t'\right)$. Next, we introduce the instantaneous firing rate $\nu_j\left(t\right)$ of neuron j. If all presynaptic neurons j belong to a homogeneous population of identical neurons with uncorrelated activity and a postsynaptic neuron i receives input from K of these neurons, the mean and variance (first and second infinitesimal moments [92]) of the input current to neuron i are given by

$$\begin{aligned} \mu_i\left(t\right) &= \tau_\mathrm{m}\sum_j J_{ij}\,\nu_j\left(t-d\right) = \tau_\mathrm{m}JK\,\nu\left(t-d\right), \\ \sigma_i^2\left(t\right) &= \tau_\mathrm{m}\sum_j J_{ij}^2\,\nu_j\left(t-d\right) = \tau_\mathrm{m}J^2K\,\nu\left(t-d\right), \end{aligned} \tag{15}$$

where $\nu \equiv \langle\nu_j\rangle$ represents the population-averaged instantaneous firing rate.

Such a mean-field approach has been employed previously to study networks of spiking neurons without spatial structure [60, 64–66]. We extend on this approach by assuming that the neurons are placed on a discrete one-dimensional domain with an inter-neuron space constant Δx. In the continuum limit $\Delta x \ll 1$ we discard the single-neuron index i and use a continuous variable $x \in \mathbb{R}$ for space, replacing $\mu_i\left(t\right) \to \mu\left(x,t\right)$. We preserve the in-degree K and establish connections according to

the symmetric and normalized connection probability $p(r)$. As before, p depends only on distance, the absolute value of the displacement $r = x - y$ for neurons at positions x and y.

In a spatially and temporally homogeneous state we may describe the state of the system by a stationary firing rate independent of time and space: $\nu(x,t) = \nu_0$ (see Eq 50 in Methods). To investigate the stability of the spatially homogeneous stationary state, we consider a small excursion $\delta\nu$ away from the stationary firing rate ν_0,

$$\nu(x,t) = \nu_0 + \delta\nu(x,t), \qquad \delta\nu \ll \nu_0, \tag{16}$$

caused by a perturbation of the synaptic input and study its effect on the dynamics of ν. The response of the firing rate to the synaptic input can be approximated to linear order in $\delta\nu$ by applying linear response theory to the Fokker-Planck equation [93], and expressing $\delta\nu$ in terms of the temporal linear convolution kernels $h_\mu(t)$ and $h_{\sigma^2}(t)$ [94] as

$$\delta\nu(x,t) = [h_\mu * \delta\mu](x,t) + \left[h_{\sigma^2} * \delta\sigma^2\right](x,t). \tag{17}$$

The convolution operation is purely temporal, and the form of the response kernels is given in Eqs 51-53 in Methods.

As the network is recurrently connected, an excursion of the firing rate in turn leads to a perturbation of the mean of the synaptic input and its variance according to

$$\begin{aligned} \delta\mu(x,t) &= \tau_\mathrm{m} JK \int_{-\infty}^{\infty} p(x-y)\ \delta\nu(y,t-d)\ \mathrm{d}y \\ \delta\sigma^2(x,t) &= \tau_\mathrm{m} J^2 K \int_{-\infty}^{\infty} p(x-y)\ \delta\nu(y,t-d)\ \mathrm{d}y. \end{aligned} \tag{18}$$

In the following section, however, we ignore the h_{σ^2} terms because their contributions are usually small [94]. The combination of Eq 17 and Eq 18 provides a linearized system for the spiking model that is continuous in space and time and enables a direct comparison with the neural-field model in the following section.

2.6 Comparison of neural-field and spiking models

The linearization of the LIF model presented in the preceding section is the analogue to taking the derivative ψ' of the gain function in the linear stability analysis of the neural-field model in Section 2.1. Therefore the results for the neural field model carry over to the spiking case. To expose the similarities between the linearized systems of the spiking model and the neural-field model, we may bring the equations for the deviation from baseline activity

$$\delta o(x,t) = \begin{cases} \delta u(x,t) & \text{neural field} \\ \delta\nu(x,t) & \text{spiking} \end{cases} \tag{19}$$

to the form of the convolution equation

$$\begin{aligned} \delta o(x,t) &= \left[\widetilde{h} * \delta i\right](x,t) \\ \delta i(x,t) &= \int_{-\infty}^{\infty} p(x-y)\ \delta o(y,t-d)\ \mathrm{d}y, \end{aligned} \tag{20}$$

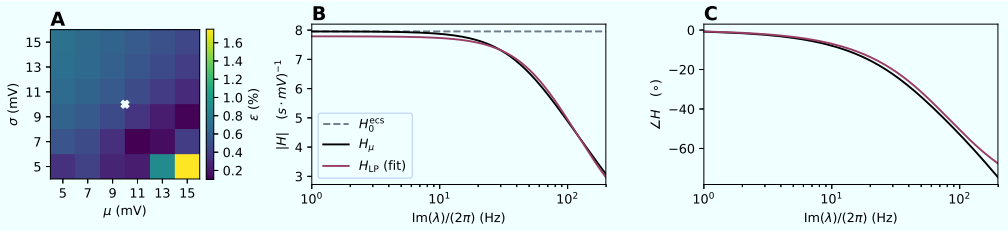

Figure 6. Transfer function of spiking neuron model and its approximation. **A** Fitting error of the low-pass filter approximation of the transfer function for LIF neurons derived in [94] over μ and σ (given relative to the reset potential). The fitting error $\epsilon = \sqrt{\epsilon_\tau^2 + \epsilon_{H_0}^2}$ is color-coded. **B** Amplitude of the transfer function and approximation (legend). Dashed line illustrates H_0 following from the analytically-determined effective coupling strength (see Eq 54 in Methods). **C** Phase. The white cross in panel A indicates the working point (μ, σ) selected for the transfer function shown in panels B and C and used in the simulations throughout the study.

where the only difference is the convolution kernel relating the deviation from the input δi to those of the output δo defined as

$$\widetilde{h}(t) := \begin{cases} \widetilde{h}^{\mathrm{nf}}(t) := \Theta(t)\,\frac{w}{\tau}\,\mathrm{e}^{-\frac{t}{\tau}} & \text{neural field} \\ \widetilde{h}^{\mathrm{s}}(t) := \tau_{\mathrm{m}} JK\, h_\mu(t) & \text{spiking.} \end{cases} \tag{21}$$

The kernel on the first line is the fundamental solution (Green's function) of the linear differential operator appearing on the left hand side of Eq 1, including the coupling weight w. As a consequence, the characteristic equations for both models result from the Fourier-Laplace ansatz $\delta o\,(x,t) = \mathrm{e}^{ikx}\mathrm{e}^{\lambda t}$ which relates the eigenvalues λ to the wave number k as

$$\widetilde{H}\,(\lambda) \cdot \mathrm{e}^{-\lambda d} \cdot \widehat{p}\,(k) = 1. \tag{22}$$

The effective transfer function $\widetilde{H}\,(\lambda)$ is defined as the Laplace transform of Eq 21 of the respective functions for the spiking model $\widetilde{h}^{\mathrm{s}}\,(t)$ and for the neural-field model $\widetilde{h}^{\mathrm{nf}}(t)$. As a result we obtain the transfer function for the neural-field model

$$\widetilde{H}^{\mathrm{nf}}\,(\lambda) = \frac{1}{1+\lambda\tau} w. \tag{23}$$

The corresponding expression for the effective spiking transfer function $\widetilde{H}^{\mathrm{s}}\,(\lambda)$ results from Eqs 51-53 in Methods.

2.6.1 Parameter mapping

So far the stability analysis shows that the characteristic equations for both the neural-field and the spiking model have the same form Eq 22 given a proper definition of the respective transfer functions. The transfer function characterizes the transmission of a small fluctuation in the input to the output of the neuron model. Because these transfer functions differ between the two models, it is a priori unclear whether their characteristic equations have qualitatively similar solutions.

The transfer function of the LIF model in the fluctuation-driven regime investigated here can, however, be approximated by a first order low-pass (LP) filter [89, 95, 96]

$$H_\mu\,(\lambda) \approx H_{\mathrm{LP}}\,(\lambda) = \frac{H_0}{1+\lambda\tau}. \tag{24}$$

This simplified transfer function is of identical form as the transfer function Eq 23 of the neural-field model, and thereby relates the phenomenological parameters w and τ of the neural-field model to the biophysically motivated parameters of the spiking model.

Fitting the absolute values of $H_{\mathrm{LP}}(\lambda)$ to $H_\mu(\lambda)$ yields values for the parameters τ and H_0. According to Eq 21, H_0 directly relates to w as

$$w = H_0 \tau_{\mathrm{m}} JK. \tag{25}$$

The goodness of the fit of this transfer function to the first-order low pass filter depends on the mean μ and variance σ of the synaptic input, as shown in Fig 6A. The color-coded error of the fit combines the relative errors from both fitting parameters: $\epsilon = \sqrt{\epsilon_\tau^2 + \epsilon_{H_0}^2}$. For the majority of working points (μ, σ) the error is $< 1\%$ but the relative errors increase abruptly towards the mean-driven regime. In this regime input fluctuations are small and the mean input predominantly drives the membrane potential towards threshold, so that the model fires regularly and the transfer function exhibits a peak close to the firing frequency [95, 96]. We here fix the working point to the parameters indicated by the white cross (see Eq 58 in Methods) for all populations, resulting in a common effective time constant τ. Here, we obtain a time constant $\tau = 1.94\,\mathrm{ms}$ which thus lies in between the synaptic time constant, $\tau_{\mathrm{s}} = 0.5\,\mathrm{ms}$, and the membrane time constant, $\tau_{\mathrm{m}} = 5\,\mathrm{ms}$, of the LIF neuron model. For these parameters, Fig 6B shows the amplitude and Fig 6C the phase of the original transfer function $H_\mu(\lambda)$ in black and the fitted transfer function $H_{\mathrm{LP}}(\lambda)$ in purple. The dashed gray line denotes H_0 obtained by computing the effective coupling strength from linear response theory, H_0^{ecs}, as a reference (see Eq 54 in Methods).

2.6.2 Linear interpolation between the transfer functions

Evaluating the characteristic equation for the neural-field model yields an exact solution for each branch of the Lambert W function, given by Eq 7. For this model we already established that the principle branch is the most unstable one. An equivalent condition is not known for the general response kernel of the LIF neuron. To asses whether we may transfer the result for the neural-field model to the spiking case, we investigate the correspondence between the two characteristic equations that are both of the form Eq 22 but with different transfer functions. For this purpose, we define an effective transfer function

$$\widetilde{H}_\alpha(\lambda) = \alpha \widetilde{H}^{\mathrm{s}}(\lambda) + (1-\alpha)\,\widetilde{H}^{\mathrm{nf}}(\lambda), \tag{26}$$

with the parameter α that linearly interpolates between the effective transfer functions of the spiking and the neural-field model: $\widetilde{H}_{\alpha=0}(\lambda) = \widetilde{H}^{\mathrm{nf}}(\lambda)$ and $\widetilde{H}_{\alpha=1}(\lambda) = \widetilde{H}^{\mathrm{s}}(\lambda)$. Fig 7 illustrates two different ways for solving the combined characteristic equation

$$\widetilde{H}_\alpha(\lambda) \cdot \mathrm{e}^{-\lambda d} \cdot \widehat{p}(k) = 1. \tag{27}$$

The first results from computing the derivative $d\lambda/d\alpha$ (see Eqs 55-57 in Methods) from the combined characteristic equation and integrating numerically with the exact solution of the neural-field model at $\alpha = 0$ for each branch b as initial condition:

$$\lambda(\alpha) = \int_0^\alpha \frac{\mathrm{d}\lambda}{\mathrm{d}\alpha}\,\mathrm{d}\alpha, \qquad \lambda(0) = \lambda_b \tag{28}$$

with

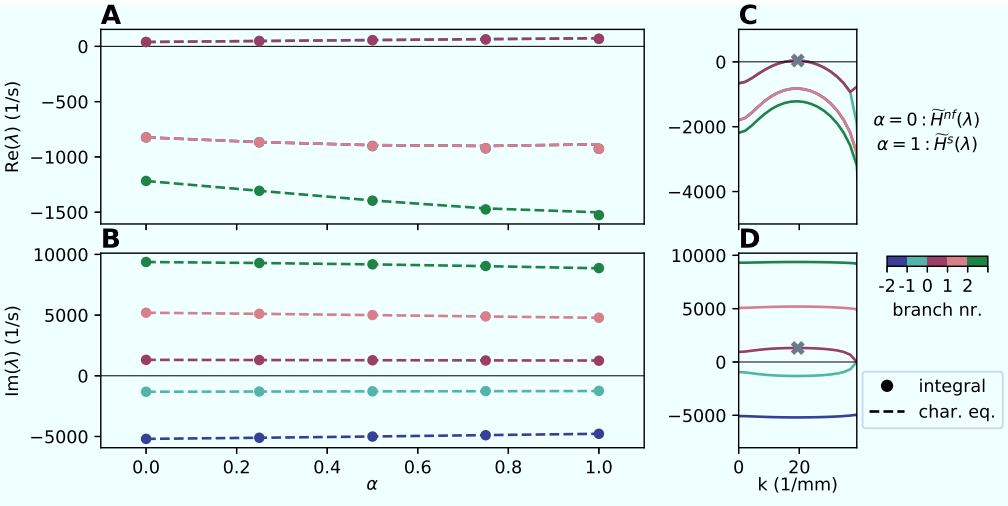

Figure 7. Linear interpolation between neural-field ($\alpha = 0$) **and spiking** ($\alpha = 1$) **model for eigenvalue close to bifurcation. A** Real and **B** imaginary part of the eigenvalue λ as a function of the linear interpolation parameter α for the characteristic equation in Eq 27. The solution at $\alpha = 0$ for the neural-field model is exact. **C** Real and **D** imaginary part of the eigenvalues (same units but different scaling as in A and B) with analytically exact solution (by Lambert W function, $\alpha = 0$) as functions of the wave number k. Different branches b are color-coded (legend); $b = 0$ corresponds to the principal branch with the maximum real eigenvalue (gray cross). Circular markers denote the linear interpolation according to the numerical integration of Eq 28. Dashed line segments for the linear interpolation are obtained by solving the characteristic equation Eq 27 numerically. Both are evaluated at the same values for α. Parameters: $d = 1.5\,\mathrm{ms}$, $R_\mathrm{E} = 0.2\,\mathrm{mm}$, $R_\mathrm{I} = 0.07\,\mathrm{mm}$, $g = 5$.

$$\frac{\mathrm{d}\lambda}{\mathrm{d}\alpha} = -\frac{\widetilde{H}^\mathrm{s}(\lambda) - \widetilde{H}^\mathrm{nf}(\lambda)}{\alpha\frac{\partial\widetilde{H}^\mathrm{s}(\lambda)}{\partial\lambda} + (1-\alpha)\frac{\partial\widetilde{H}^\mathrm{nf}(\lambda)}{\partial\lambda} - d\cdot\widetilde{H}_\alpha(\lambda)}. \tag{29}$$

The spatial profile only enters the initial condition, and the derivative Eq 29 is independent of the wave number k.

As an alternative approach, we directly solve the combined characteristic equation Eq 27 numerically with the known initial condition. Fig 7A and B indicate that only the principle branch ($b = 0$) becomes positive while the other branches remain stable. The branches come in complex conjugate pairs. For the numerical solution of the characteristic equation, we fix the wave number to the value of k that corresponds to the maximum real eigenvalue.

The analysis shows that we may ignore the danger of branch crossing since different branches remain clearly separated in Fig 7A and B. In addition, the eigenvalue on the principle branch is mostly independent of α, even if the system is close to the bifurcation (when the real part of λ_0 is close to zero). Thus for all values of α we expect qualitatively similar bifurcations, including $\alpha = 1$. This justification transfers the rigorous results from the bifurcation analysis of the neural-field model in Section 2.2 and Section 2.3, and corresponding effective parameters, to the spiking model.

2.7 Validation by simulation of spiking neural network

The Introduction illustrates spatiotemporal patterns emerging in a spiking network simulation in Fig 1 and the subsequent sections derive a theory describing the mechanisms underlying such patterns. Finally, the parameter mapping between the spiking and the neural-field model explains the origin of the spike patterns by transferring the conditions found for the abstract neural-field model in Section 2.2 and Section 2.3 to the spiking case. This section validates that the correspondence between network parameters in the two models is not incidental but covers the full phase diagram.

In the following, we simulate a network with the same neural populations and spatial connectivity used in the nonlinear rate-network in Fig 5, but replace the rate-model neurons by spiking neurons, and map the parameters as described in Section 2.6.1. The network model characterizes all neurons by the same working point (see Eq 58 in Methods), which means that the connectivity matrix for the excitatory-inhibitory network has equal rows; entries in Eq 4 depend on the presynaptic population alone. Therefore the relative in-degree $\gamma = K_\mathrm{I}/K_\mathrm{E}$ and the relative synaptic strength $g = -J_\mathrm{I}/J_\mathrm{E}$ parametrize the spiking-network connectivity matrix as

$$P(r) = \tau_m J_\mathrm{E} K_\mathrm{E} \begin{pmatrix} p_\mathrm{E}(r) & -\gamma g\, p_\mathrm{I}(r) \\ p_\mathrm{E}(r) & -\gamma g\, p_\mathrm{I}(r) \end{pmatrix}. \tag{30}$$

The rightmost panels of Fig 8A-C show the same simulation results as Fig 1B-D; likewise the panels of Fig 1 have parameters that correspond to those of the rate-neuron network in Fig 5. The different patterns in Fig 1B-D emerge by gradually shifting a single network parameter that switches the system from a stable state (white filled markers in Fig 8D and E), across intermediate states (gray-scale filled markers) to the final states where stability is lost and the patterns have formed (black filled markers). Arrows visualize the sequences in the phase diagrams Fig 8D and E and the markers reappear in the upper left corners of the corresponding raster plots in Fig 8A-C.

The sequence of panels in Fig 8A illustrates a gradual transition from a stable (AI) state to spatial oscillations attained by increasing the amplitudes of excitatory postsynaptic current (PSC) amplitudes $J_\mathrm{E}^{'}$ in the network. With $J^{'}$ we denote the weight as a jump in current while J denotes a jump in voltage in the physical sense, and the relationship is: $J^{'} = C_\mathrm{m} J/\tau_s$ (see Eq 60 in Methods). The parameter variation thus homogeneously scales the effective profile $\widehat{P}$ but preserves the shape of the reduced profile $\widehat{B}$ (fixed position of diamond marker in panel F). Simultaneously an increasing rate of the external Poisson input compensates for the reduced PSC amplitudes to maintain the fixed working point (μ, σ) of the neurons (see Eq 58 in Methods). Diamond markers in Fig 8D show that along its path the system crosses the critical value $\widehat{P}_\mathrm{max} = 1$, while $\widehat{P}_\mathrm{min} > \widehat{P}_\mathrm{min}^\mathrm{crit}(\tau/d^\mathrm{crit})$ stays in the stable regime, as shown in panel E. However, even for $\widehat{P}_\mathrm{max} \lesssim 1$ (for $J_E^{'} = 60\,\mathrm{pA}$) the network activity already exhibits weak spatial oscillations.

Choosing the synaptic delay d as a bifurcation parameter highlights the onset of temporal oscillations for the case $k = 0$ (panel B sequence, circular markers) and spatiotemporal oscillations for the case $k > 0$ (sequence in Fig 8C, star markers). In contrast to the case of purely spatial waves in panel A, the procedure preserves the effective spatial profile (fixed positions in panels D and F) and the system crosses the transition curve in panel E due to increasing delay alone, thus decreasing the ratio τ/d.

Fig 8C illustrates the gradual transition to traveling waves, where $\widehat{P}_\mathrm{max}$ remains in the theoretically stable regime at all times, but is close to the critical value of 1 (see

the star marker in panel D). As a result, we observe spatial oscillations with a spatial frequency given by $k_{\max}$ before and even after the Hopf bifurcation. For delays longer than the critical delay, mixed states occur in which different instabilities due to $\widehat{P}_{\max}$ and $\widehat{P}_{\min}$ compete. For delay values well past the bifurcation, this mixed state is lost resulting in a dependency only on $\widehat{P}_{\min}$ and periodic traveling waves with a spatial frequency that depends on $k_{\min}$.

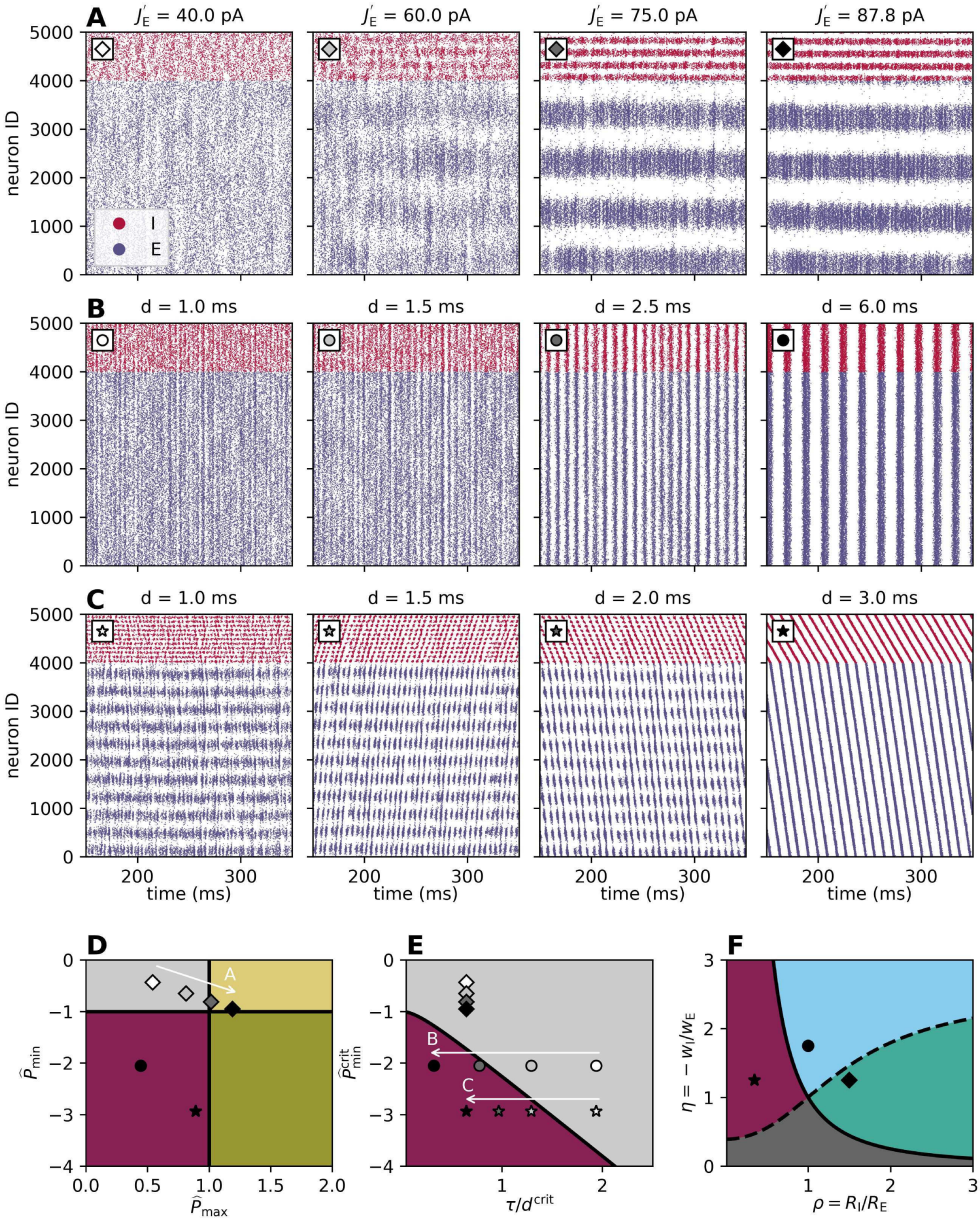

Figure 8. Transitions from theoretically stable states to spatiotemporal patterns in spiking network simulation. A-C Spike rasters showing transition to network states in Fig 1B-D (same markers, same parameter combinations). The changed parameter value is given on top of each raster plot. **A** Increasing recurrent weight J_E' leads to onset of spatial oscillations. **B** Increasing synaptic delay d leads to onset of temporal oscillations at $k = 0$. **C** Increasing delay d leads to onset of temporal oscillations at $k > 0$, i.e., periodic traveling waves. **D-E** Gray shaded markers and white arrows labeled according to respective panel A-C in phase diagrams indicate sequences of parameter combinations and breakdown of stability at $\widehat{P}_{\max} = 1$ or at $\widehat{P}_{\min} = \widehat{P}_{\min}^{\text{crit}}$. For each sequence in panels A-C, delay d, excitatory profile width R_E, inhibitory profile width R_I, and the relative synaptic strength g correspond to the values given in Fig 1B-D with corresponding markers.

3 Discussion

The present study employs mean-field theory [60] to rigorously map a spiking network model of leaky integrate-and-fire (LIF) neurons with constant transmission delay to a neural-field model. We use a conceptually similar linearization as Kriener et al. [85] combined with an analytical expressions for the transfer function in the presence of colored synaptic noise [94]. The insight that this transfer function in the fluctuation-driven regime resembles the one of a simple first-order low-pass filter facilitates the parameter mapping between the two models. The resulting analytically tractable effective rate model depends on the dynamical working point of the spiking network that is characterized by both the mean and the variance of the synaptic input. By means of bifurcation theory, in particular linear Turing instability analysis [29, 44, 45], we investigate the origin of spatiotemporal patterns such as temporal and spatial oscillations and in particular periodic traveling waves emerging in spiking activity. The mechanism underlying these waves encompasses delay-induced fast global oscillations, as described by Brunel and Hakim [60], with spatial oscillations due to a distance-dependent effective connectivity profile. We derive analytical conditions for pattern formation that are exclusively based on general characteristics of the effective connectivity profile and the delay. The profile is split into a static weight that is either excitatory or inhibitory for a given neural population, and a spatial modulation that can be interpreted as a distance-dependent connection probability. Given the biological constraint that connection probabilities depend on distance but weights do not, periodic traveling waves cannot occur in a single homogeneous population irrespective of the shape of distance-dependent connection probability. Only the effective connectivity profile of two populations (excitatory and inhibitory), permits solutions where a mode with finite non-zero wave number is the most unstable one, a prerequisite for the emergence of nontrivial spatial patterns such as traveling waves. We therefore establish a relation between the anatomically measurable connectivity structure and observable patterns in spiking activity. The predictions of the analytically tractable neural-field model are validated by means of simulations of nonlinear rate-unit networks [97] and of networks composed of LIF-model neurons, both using the same simulation framework [98]. In our experience, the ability to switch from a model class with continuous real-valued interaction to a model class with pulse-coupling by changing a few lines in the formal high-level model description increases the efficiency and reliability of the research.

The presented mathematical correspondence between these a priori distinct classes of models for neural activity has several implications. First, as demonstrated by the application in the current work, it facilitates the transfer of results from the well-studied domain of neural-field models to spiking models. The insight thus allows the community to arrive at a coherent view of network phenomena that appear robustly and independently of the chosen model. Second, the quantitative mapping of the spiking model to an effective rate model in particular reduces the parameters of the former to the set of fewer parameters of the latter; single-neuron and network parameters are reduced to just a weight and a time constant. This dimensionality reduction of the parameter space conversely implies that entire manifolds of spiking models are equivalent with respect to their bifurcations. Such a reduction supports systematic data integration: Assume a researcher wants to construct a spiking model that reproduces a certain spatiotemporal pattern. The presented expressions permit the scientist to restrict further investigations to the manifold in parameter space in line with these observations. Variations of parameters within this manifold may lead to phenomena beyond the predictions of the initial bifurcation analysis. Additional constraints, such as firing rates, degree of irregularity, or correlations, can then further reduce the set of admissible parameters.

To keep the focus on the transferability of results from a neural-field to a spiking model, the study restricts the analysis to a rather simple network model. In many cases, extensions to more realistic settings are straight forward. As an example, we perform our analysis in one-dimensional space. In two dimensions, the wave number becomes a vector and bifurcations to periodic patterns in time and space can be constructed (see [28, Section 8.4] and [29]). Likewise, we restricted ourselves to a constant synaptic delay like Roxin et al. [42, 51] because it enables a separation of a spatial component, the shape of the spatial profile, and a temporal component, the delay. A natural next step is the inclusion of an axonal distance-dependent delay term as for instance in [40] to study the interplay of both delay contributions [58]. For simplification, we use here a boxcar-shaped spatial connectivity profile in the demonstrated application of our approach. For the emergence of spatiotemporal patterns, however, the same conditions on the connectivity structure and the delays hold for more realistic exponentially decaying or Gaussian-shaped profiles [20–22]. If the spatial connectivity profiles are monotonically decaying in the Fourier domain (as it is the case for exponential or Gaussian shapes), the Fourier transform of the effective profile of a network composed of an excitatory and an inhibitory population exhibits at most one zero-crossing. Either the minimum or the maximum are attained at a non-zero and finite wave number k, but not both. With a cosine-shaped effective profile, only a single wave number dominates by construction [42, 51]. Here, we decided for the boxcar shape because of its oscillating Fourier transform that allows us to study competition between two spatial frequencies corresponding to the two extrema.

Similar to our approach, previous neural-field studies describe the spatial connectivity profile as a symmetric probability density function (see, for example, [49]). For our aim, to establish a link to networks of discrete neurons, the interpretation as a connection probability and the separation from a weight are a crucial addition. This assumption enables us to distinguish between different neural populations, to analyze the shape of the profile based on parameters for the excitatory and the inhibitory contribution, and to introduce biophysically motivated parameters for the synaptic strength. Starting directly with an effective profile that includes both, excitation and inhibition, such as (inverse) Mexican hat connectivity, is mathematically equivalent and a common approach in the neural-fields literature [29, 40, 42, 53]. But it neglects the biological separation of neurons into excitatory and inhibitory populations according to their effect on postsynaptic targets (Dale's law [99]) and their different spatial reach of connectivity [100]. A result of this simplification, these models can produce waves even with a single homogeneous population [42–44], while with homogeneous stationary external drive we show that at least two populations are required.

Local excitation and distant inhibition are often used to support stationary patterns such as bumps, while local inhibition and distant excitation are associated with non-stationary patterns such as traveling waves [28, 40, 101]. For sufficiently long synaptic delays, we also observe periodic traveling waves with local inhibition and distant excitation, as often observed in cortex [100]. However, we show that the reason for this is the specific shape of the effective spatial profile, and not only the spatial reach itself. Our argumentation is therefore in line with Hutt et al. [48, 54] who demonstrate that wave instabilities can even occur with local excitation and distant inhibition for specific spatial interactions. The spatial connectivity structure and related possible activity states are in addition important factors for computational performance or function of model networks [84, 102].

The parameter mapping between a neural-field and a spiking model in this study relies on the insight that the transfer function of the LIF neuron in the fluctuation-driven regime resembles the one of a simple first-order low-pass filter.

Since this approximation not only holds for LIF neurons, but also for other spiking neuron models, our results are transferable. A further candidate model with this property is the exponential integrate-and-fire model [103]. Other examples include Nordlie et al. [104] who characterize the firing-rate responses of LIF neurons with strong alpha-shaped synaptic currents and similarly Heiberg et al. [105] for a LIF neuron model with conductance based synapses and potassium-mediated afterhyperpolarization currents previously proposed [106].

In the literature, the time constant of neural-field models is often associated with the membrane or the synaptic time constant [33, 73, 84]. Here, we observe that the time constant of the neural-field model derived from the network of spiking neurons falls in between the two. In line with [104, 107], we suggest to reconsider the meaning of the time constant in neural-field models.

A limitation of the approach employed here is that the linear theory is only exact at the onset of waves. Beyond the bifurcation, it is possible that nonlinearities in the spiking model govern the dynamics and lead to different prevailing wave numbers or wave frequencies than predicted. Roxin et al. [51] report that the stability of traveling waves depends crucially on the nonlinearity. Nevertheless they do not observe traveling waves in their spiking-network simulations. In the present work, however, we identify biophysically motivated neuron and network parameters that allow traveling waves to establish in a spiking network. Still, we had to increase the delay beyond the predicted bifurcation point to obtain a stable wave pattern.

Furthermore, the theory underlying the mapping of the spiking network to the neural-field model is based on the diffusion approximation and therefore only applicable for sufficiently small synaptic weights. Widely distributed synaptic weights, for example, may lead to larger deviations. We here primarily target a wave-generating mechanism for cortical networks. Since in other brain regions involved neuron types, connectivity structures and input characteristics are different, other mechanisms for pattern formation not covered in this work need to be taken into account [3].

The working-point dependence of the neural-field models derived here offers a new interpretation of propagating activity measured in vivo [8, 12]. Even if the anatomical connectivity remains unchanged during a period of observation, the stability of the neural system can be temporarily altered due to changes in activity. The transfer function of a LIF neuron depends on the mean and the variance of its input, and we have shown that stability is related to its parametrization. In particular, local changes of activity, for example due to a spatially confined external input, can affect stability and hence influence whether a signal remains rather local or travels across the cortical surface. That means, we would relate the tendency of a neural network to exhibit spatiotemporal patterns not only to its connectivity, but also to its activity state that can change over time.

4 Methods

4.1 Linear stability analysis

4.1.1 Derivation of the characteristic equation

With the Fourier-Laplace ansatz $u(x,t) = e^{\mathrm{i}kx}\mathrm{e}^{\lambda t}$ for the integro-differential equation in Eq 1 linearized around u_0 and the choice to set the slope of the gain function to unity, the characteristic equation in Eq 3 results from

$$\begin{aligned}
\tau\lambda\,\mathrm{e}^{ikx}\mathrm{e}^{\lambda t} &= -\mathrm{e}^{ikx}\mathrm{e}^{\lambda t} + \int_{-\infty}^{\infty} wp\,(x-y)\,\mathrm{e}^{iky}\mathrm{e}^{\lambda(t-d)}\,\mathrm{d}y \\
\tau\lambda &= -1 + w\mathrm{e}^{-\lambda d}\int_{-\infty}^{\infty} p\,(x-y)\,\mathrm{e}^{-ik(x-y)}\,\mathrm{d}y \\
&= -1 - w\mathrm{e}^{-\lambda d}\int_{\infty}^{-\infty} p\,(r)\,\mathrm{e}^{-ikr}\,\mathrm{d}r, \qquad r = x-y \\
&= -1 + w\mathrm{e}^{-\lambda d}\underbrace{\int_{-\infty}^{\infty} p\,(r)\,\mathrm{e}^{-ikr}\,\mathrm{d}r}_{\equiv\widehat{p}(k)}.
\end{aligned} \tag{31}$$

In the last row, we recognize the Fourier transform $\widehat{p}$ of the spatial profile p.

4.1.2 Effective connectivity profile for two populations

While the connectivity P is a scalar in the one-population model, it is a matrix in the case of two populations (given in Eq 4). The ansatz for deriving the characteristic equation in the latter case reads $\delta u\,(x,t) = v\mathrm{e}^{ikx}\mathrm{e}^{\lambda t}$, with v denoting a vector of constants. This leads to the auxiliary eigenvalue problem

$$\widehat{P}\,(k)\;v = \widetilde{P}\,(k)\;v, \tag{32}$$

where $\widehat{P}$ denotes an eigenvalue and $\widetilde{P}$ is an auxiliary matrix containing the Fourier transforms of the entries of P:

$$\widetilde{P}\,(k) = \begin{pmatrix} w_{\mathrm{EE}}\,\widehat{p}_{\mathrm{EE}}\,(k) & w_{\mathrm{EI}}\,\widehat{p}_{\mathrm{EI}}\,(k) \\ w_{\mathrm{IE}}\,\widehat{p}_{\mathrm{IE}}\,(k) & w_{\mathrm{II}}\,\widehat{p}_{\mathrm{II}}\,(k) \end{pmatrix}. \tag{33}$$

Eq 32 possesses a nontrivial solution v if and only if $\det\left(\widetilde{P}\,(k) - \widehat{P}\,(k)\,\mathbb{1}\right) = 0$. Eq 5 explicitly states the two eigenvalues $\widehat{P}_{1,2}$ solving this equation. These eigenvalues constitute the effective profile in the characteristic equation in Eq 3 that hence holds also for the two-population case.

4.1.3 Largest real part on principle branch of Lambert W function

The function $x\,(W) = W\,\mathrm{e}^{W}$ has a minimum at $W = -1$, no real solution for $x < -\mathrm{e}^{-1}$, a single solution for $x > 0$, and two solutions for $x \in [-e^{-1}, 0)$. Typically, the term 'principal branch' of the Lambert W function with branch number $b = 0$ refers to the real branch defined on the interval $[-e^{-1}, \infty)$, where for negative arguments the larger solution is considered. Here we extend the definition to the whole real line by the complex branch with maximal real part and positive imaginary part on $(-\infty, -e^{-1})$.

We demonstrate that the branch of the Lambert W function with the largest real part is the principal branch. Considering only real-valued arguments $x \in \mathbb{R}$, we write $W\,(x) = |W\,(x)|\,\mathrm{e}^{i\varphi} = \alpha + i\beta$ and

$$W\,(x)\,\mathrm{e}^{W(x)} = |W\,(x)|\;\mathrm{e}^{\alpha}\,\mathrm{e}^{i(\varphi+\beta)} = x \in \mathbb{R} \tag{34}$$

$$\rightarrow \mathrm{e}^{i(\varphi+\beta)} = \pm 1, \tag{35}$$

where $\varphi \in [-\pi, \pi]$ is the principal value. We index the branches by $q \in \mathbb{Z}$ according to the number of half-cycles of the exponential in Eq 35: $\varphi + \beta = q \cdot \pi$. The branch

number is equal to $b = \left\lfloor \frac{q}{2} \right\rfloor$ with $\lfloor \cdot \rfloor$ denoting the floor function. The principle branch is therefore given by the index $q = 0$ for $x \geq 0$ and by $q = 1$ for $x < 0$.

Taking the absolute square of Eq 34 yields the real equation

$$x^2 \, \mathrm{e}^{-2\alpha} = \alpha^2 + \beta^2. \tag{36}$$

Without loss of generality we may assume $\beta \geq 0$; this is certainly true for the real solutions with $\beta = 0$ and it also holds for one of the complex solutions for any complex pair. Complex solutions come in conjugate pairs due to the symmetry $(\varphi, \beta) \to (-\varphi, -\beta)$ exhibited by Eq 35 and Eq 36. Since each member of a pair has by definition the same real part, it is sufficient to consider only the member with positive imaginary part $\beta > 0$.

To prove that the real part α of W is maximal for $b = 0$, we show that α is a decreasing function of β along the solutions of Eq 34. Investigating the intersections of the left-hand side and the right-hand side of Eq 36 as a function of α illustrates how increasing the imaginary part β affects the real part α. The left-hand side is a decaying function of α with an intercept of x^2. The right-hand-side is a parabola with an offset of β^2.

For $x \in (-\infty, -e^{-1}) \cup [0, \infty)$, an intersection occurs either at a positive real part $\alpha \geq 0$ if $x^2 \geq \beta^2$, or at a negative real part $\alpha < 0$ if $x^2 < \beta^2$. Increasing β moves the parabola upwards and therefore the intersection to the left, meaning that α decreases with increasing β.

For $x \in [-e^{-1}, 0)$, we distinguish the cases $\beta = 0$ and $\beta > 0$ which both have only solutions with $\alpha < 0$. First, the two real solutions ($q = \pm 1$) existing in this interval correspond to two simultaneously occurring intersections; in addition a third intersection is created by the squaring Eq 36 but it is not an actual solution of Eq 34. The intersection at the larger real part per definition corresponds to the principal branch with index $q = 1$. Second, the complex solutions are indexed by odd numbers q with $|q| > 1$. Taking into account the interval where φ is defined, the imaginary part is bounded from below such that $\beta \geq 2\pi$ for non-principal branches. Analogous to the previously discussed interval of x, there exists only one intersection between the exponential function and the parabola for large values of β (in particular: $x^2 < \beta^2$) that moves towards smaller values of α with increasing β.

So in summary we have shown that for real x, the principal branch harbors the solutions with maximal real part α.

4.1.4 Characteristic equation with Lambert W function

The characteristic equation in Eq 3 can be rewritten in terms of the Lambert W function to Eq 7 using the transformation:

$$\begin{aligned} (1 + \tau\lambda) \, \mathrm{e}^{\lambda d} &= \widehat{P}(k) \mid \cdot \frac{d}{\tau} \mathrm{e}^{\frac{d}{\tau}} \\ \left(d\lambda + \frac{d}{\tau} \right) \mathrm{e}^{d\lambda + \frac{d}{\tau}} &= \widehat{P}(k) \, \frac{d}{\tau} \mathrm{e}^{\frac{d}{\tau}} \\ d\lambda + \frac{d}{\tau} &= W\left(\widehat{P}(k) \, \frac{d}{\tau} \mathrm{e}^{\frac{d}{\tau}} \right). \end{aligned} \tag{37}$$

The last step collects terms using the definition of the Lambert W function, $z = W(z) \, \mathrm{e}^{W(z)}$ with $z \in \mathbb{C}$.

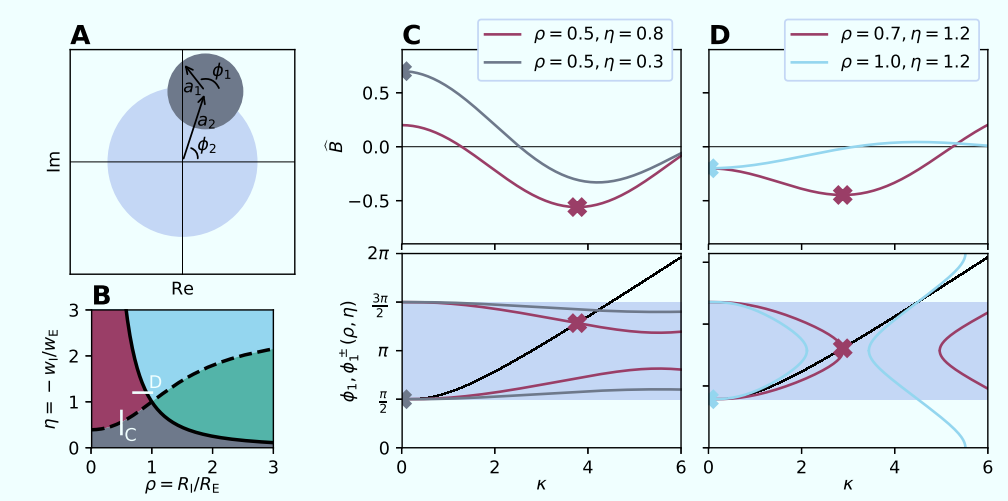

Figure 9. Graphical analysis for extrema of reduced profile for derivation of transition curves. A The condition for the extremum Eq 41 amounts to the addition of two vectors in the complex plane whose sum is purely imaginary. The vectors have lengths a_1 and a_2 and angles ϕ_1 and ϕ_2, defined in Eq 42. **B** Diagram of Fig 3F with indicated parameter combinations (ρ, η) as used in panels C and D. **C-D** Reduced profile $\widehat{B}$ (top) and ϕ_1 and $\phi_1^{\pm}$ from Eq 43 vs. κ (bottom) for two different combinations of (ρ, η) with line colors corresponding to regions in panel B. **C** $\left|\widehat{B}_{\min}\right| > \widehat{B}_{\max}$ in purple and vice versa in dark gray. **D** $\widehat{B}_{\min}$ at $\kappa = 0$ in light blue and at $\kappa > 0$ in purple.

4.2 Properties of the spatial profile

We assume that the spatial profile p is a symmetric probability density function, which implies that its Fourier transform $\widehat{p}$, also called the characteristic function, is real valued and even. Further, we can prove that $\widehat{p} \in (-1, 1]$ and that $\widehat{p}$ attains 1 only at the origin in two steps:

- $|\widehat{p}(k)| \leq 1$ for all $k \in \mathbb{R}$:

$$\begin{aligned} |\widehat{p}(k)| &= \left| \int_{-\infty}^{\infty} p(r) \mathrm{e}^{-ikr} \, \mathrm{d}r \right| \leq \int_{-\infty}^{\infty} \left| p(r) \mathrm{e}^{-ikr} \right| \, \mathrm{d}r \\ &= \int_{-\infty}^{\infty} p(r) \, \mathrm{d}r = 1 \quad \text{for all } k \in \mathbb{R}, \end{aligned} \tag{38}$$

- $|\widehat{p}(k)| < 1$ for all $k \neq 0$:

$$\begin{aligned} \left| \int_{-\infty}^{\infty} p(r) \mathrm{e}^{-ikr} \mathrm{d}r \right| &\leq \int_{-\infty}^{\infty} p(r) \left| \cos(kr) \right| \, \mathrm{d}r \\ &< \int_{-\infty}^{\infty} p(r) \, \mathrm{d}r = 1 \quad \text{for all } k \neq 0, \end{aligned} \tag{39}$$

because $|\cos(kr)| < 1$ almost everywhere in r if $k \neq 0$.

4.3 Transition curves for reduced profile

We here use a graphical approach to derive the transition curves shown first in Fig 3F. A necessary condition for an extreme value of the reduced profile $\widehat{B}(\kappa)$ from Eq 12 located at κ^* is: $\frac{\partial}{\partial \kappa} \widehat{B}(\kappa)|_{\kappa^*} = 0$. With the derivative

$$\frac{\partial}{\partial\kappa}\widehat{B}\left(\kappa\right)=\frac{\cos\left(\kappa\right)}{\kappa}-\frac{\sin\left(\kappa\right)}{\kappa^2}-\eta\frac{\cos\left(\rho\kappa\right)}{\kappa}+\eta\frac{\sin\left(\rho\kappa\right)}{\rho\kappa^2}, \tag{40}$$

this condition can be rewritten as

$$\begin{aligned}0&=\mathrm{Re}\left[\left(\kappa+i\right)\mathrm{e}^{i\kappa}-\frac{\eta}{r}\left(\rho\kappa+i\right)\mathrm{e}^{i\rho\kappa}\right]\\&=\mathrm{Re}\left[a_1\mathrm{e}^{i\phi_1}+a_2\mathrm{e}^{i\phi_2}\right]\\&=a_1\cos\left(\phi_1\right)+a_2\cos\left(\phi_2\right),\end{aligned} \tag{41}$$

where a_1 and a_2 are the absolute values of the complex numbers and ϕ_1 and ϕ_2 their phases, given by

$$\begin{aligned}a_1\left(\kappa\right)&=\sqrt{1+\kappa^2}\\\phi_1\left(\kappa\right)&=\kappa+\frac{\pi}{2}-\arctan\left(\kappa\right)\\a_2\left(\kappa;\rho,\gamma\right)&=\frac{\eta}{\rho}\sqrt{1+\rho^2\kappa^2}\\\phi_2\left(\kappa;\rho\right)&=\rho\kappa+\frac{3\pi}{2}-\arctan\left(\rho\kappa\right).\end{aligned} \tag{42}$$

The vanishing right-hand-side of Eq 41 implies that the term in the square brackets is purely imaginary. An example solution for the case $a_1 < a_2$ is illustrated in Fig 9A in the complex plane. Note that a_1 and ϕ_1 are independent of the parameters ρ and η in this representation. In our graphical analysis, Eq 41 is interpreted as the sum of two vectors in the complex plane. As shown in Fig 9A, we determine ϕ_1 as the angle at which the tip of the second vector ends on the imaginary axis, which follows from elementary trigonometry as

$$\phi_1^{\pm}=\pi\pm\arccos\left(\frac{a_2}{a_1}\cos\left(\phi_2\right)\right). \tag{43}$$

The locations of extrema are then given by the intersections of $\phi_1^{\pm}$ with the second row of Eq 42. Here ϕ_2 is determined from the last equation in Eq 41.

Fig 9B reproduces Fig 3F. The white bars connect points given by parameter combinations (ρ,η) on both sides of the transition curves, and the parameters are specified in panels C and D. The first transition curve $\eta_{t1}\left(\rho\right)$ (dashed line in Fig 9B) is determined by $\widehat{B}_{\max}\left(\kappa_{\max}\right)=\left|\widehat{B}_{\min}\left(\kappa_{\min}\right)\right|$, that means it is determined by parameters (ρ,η) for which the absolute values of the positive and negative extremum of the profile are equal. The top panel of Fig 9C compares two reduced profiles obtained for a fixed value for ρ and two values for η. The line colors correspond to the colored regions in the diagram in Fig 9B for the respective parameter combination $\left|\widehat{B}_{\min}\right|>\widehat{B}_{\max}$ for the purple profile and vice versa for the dark gray profile. The point with the maximum absolute value of each profile is indicated with a cross. Exactly at the transition either $\kappa_{\max}$ or $\kappa_{\min}$ is zero (for example $\kappa_0=0$) and the other one is non-zero (for example $\kappa_1>0$). This condition, with Eq 12, yields the absolute value for both extrema at the transition, where they must be equal, thus $\left|\widehat{B}\left(\kappa_0\right)\right|=\left|\widehat{B}\left(\kappa_1\right)\right|=|1-\eta|$. Any point on the transition curve is a unique triplet of parameters(ρ,η,κ_1), and with the condition $\frac{\partial}{\partial\kappa}\widehat{B}\left(\kappa\right)|_{\kappa_1}=0$ we obtain two equations that need to be fulfilled at each point for $\kappa=\kappa_1$:

$$\begin{aligned} 1-\eta &= \frac{\sin(\kappa)}{\kappa} - \eta\frac{\sin(\rho\kappa)}{\rho\kappa} \\ 1-\eta &= \cos(\kappa) - \eta\cos(\rho\kappa)\,. \end{aligned} \tag{44}$$

The lower equation is obtained by identifying $\widehat{B}(\kappa)$ in its derivative in Eq 40. We solve both equations with respect to η and equate them to get

$$\frac{1}{\kappa}\sin(\kappa)\left[1+\cos(\rho\kappa)\right] - \frac{1}{\rho\kappa}\sin(\rho\kappa)\left[1+\cos(\kappa)\right] + \cos(\rho\kappa) - \cos(\kappa) = 0. \tag{45}$$

For a given value of ρ, we compute the roots of the left-hand-side expression, which defines $\kappa(\rho)$. The bottom panel of Fig 9C shows ϕ_1 from Eq 42 as a black line and $\phi_1^{\pm}$ from Eq 43 for the parameters of the two effective profiles (same color coding as in the top panel). The intersections corresponding to the relevant extrema are highlighted by crosses. This visual analysis allows us to identify the interval for κ in which zero-crossings of the left-hand side of Eq 45 as a function of κ can correspond to the extrema, that is $\kappa \in (0,\, 4.49341)$ where the lower limit corresponds to $\phi_1 = \frac{\pi}{2}$ and the upper limit to $\phi_1 = \frac{3\pi}{2}$. The zero-crossing at the smallest non-zero κ indicates the extremum at κ_1. Finally, the transition curve is given by

$$\eta_{t1}(\rho) = \frac{1+\cos(\kappa(\rho))}{1+\cos(\rho\kappa(\rho))}, \tag{46}$$

where $\kappa(\rho)$ is given by the roots of (45).

The second transition curve $\eta_{t2}(\rho)$ (solid line in Fig 9B) indicates whether the extremum with the largest absolute value occurs at $\kappa = 0$ or at $\kappa > 0$. Fig 9D shows in the top panel two reduced profiles for a fixed value of η, but two values for ρ such that the $\widehat{B}_{\min}$ occurs once at $\kappa_{\min} = 0$ (light blue as in Fig 9B) and once at $\kappa_{\min} > 0$ (purple as in Fig 9B), indicated by cross markers.

Graphical analysis using the bottom panel of Fig 9D indicates that this transition happens when ϕ_1^- at $\kappa \gtrsim 0$ switches from lying slightly above (light blue line) to below (purple line) the parameter-independent function ϕ_1 (black line). We observe that decreasing ρ moves the intersection point and with it the location of the extremum up the black line, starting from $\kappa = 0$ to larger values for κ.

Close to the transition, the intersection point comes arbitrarily close to $\kappa = 0$, which permits local analysis by a Taylor expansion of ϕ_1 for small κ:

$$\phi_1(\kappa) \approx \frac{\pi}{2} + \frac{\kappa^3}{3} + \mathcal{O}\left(\kappa^5\right) \tag{47}$$

$$\phi_1^-(\kappa;\rho,\eta) \approx \frac{\pi}{2} + \frac{\eta\rho\kappa^3}{3} + \mathcal{O}\left((\rho\kappa)^5\right). \tag{48}$$

A comparison of the coefficients of the third-order polynomials then gives the transition curve

$$\eta_{t2}(\rho) = \frac{1}{\rho^2}, \tag{49}$$

because this coefficient decides for small κ whether ϕ_1 (black line) or ϕ_1^- as a function of the parameters (ρ,η) has a larger slope and lies on top.

4.4 Linearization of the spiking model

4.4.1 Stationary firing rate

The stationary firing rate ν_0 in the limit of short synaptic time constants ($\tau_\mathrm{s} \ll \tau_\mathrm{m}$) is given by [89, 108, Eq A.1]:

$$\begin{aligned} \nu_0^{-1} &= \tau_\mathrm{r} + \tau_\mathrm{m}\sqrt{\pi}\left(F\left(y_\theta\right) - F\left(y_\mathrm{r}\right)\right) \\ f\left(y\right) &= \mathrm{e}^{y^2}\left(1+\mathrm{erf}\left(y\right)\right), \qquad F\left(y\right) = \int^y f\left(y\right) dy \\ \text{with} \quad y_{\{\theta,r\}} &= \frac{V_{\{\theta,r\}} - \mu}{\sigma} + \frac{\beta}{2}\sqrt{\frac{\tau_\mathrm{s}}{\tau_\mathrm{m}}}, \qquad \beta = \sqrt{2}\left|\zeta\left(\frac{1}{2}\right)\right|, \end{aligned} \tag{50}$$

where ζ denotes the Riemann's zeta function [109].

4.4.2 Transfer function

The transfer function here denoted by H_μ is computed based on the first term of [94, Eq 29]

$$H_G\left(\omega\right) = \frac{\nu_0\frac{\sqrt{2}}{\sigma}}{1+i\omega\tau_\mathrm{m}} \frac{\Phi'_\omega|_{x\theta}^{x_\mathrm{r}}}{\Phi_\omega|_{x\theta}^{x_\mathrm{r}}}, \tag{51}$$

for the oscillation frequency ω and $x_{\{\mathrm{r},\theta\}} = \sqrt{2}y_{\{\theta,r\}}$. The function $\Phi_\omega\left(x\right) = e^{\frac{1}{4}x^2}\,U\left(i\omega\tau_\mathrm{m} - \frac{1}{2}, x\right)$ is defined by parabolic cylinder functions U [95, 109] and $\Phi'_\omega = \partial_x\Phi_\omega$. We need to multiply the transfer function with the transfer function of a first-order low-pass filter due to the exponential time course of our synaptic currents:

$$H_\mu\left(\omega\right) = H_G\left(\omega\right)\,\frac{1}{1+i\omega\tau_\mathrm{s}}. \tag{52}$$

We then obtain h_μ by an inverse Fourier transform and a Laplace transform because λ is a complex frequency and ω is real in the present context:

$$\begin{aligned} h_\mu\left(t\right) &= \mathcal{F}^{-1}\left[H_\mu\right]\left(t\right) \\ H_\mu\left(\lambda\right) &= \mathcal{L}\left[h_\mu\right]\left(\lambda\right). \end{aligned} \tag{53}$$

The latter relations imply a replacement $i\omega \to \lambda$ in Eq 51.

4.5 Model comparison

4.5.1 Effective coupling strength

For the numerical evaluation of the transfer function, we show $H_0^\mathrm{ecs} = w^\mathrm{ecs}/\left(\tau_\mathrm{m}JK\right)$ as the dashed line in Fig 6B, obtained by calculating analytically the effective coupling strength w^ecs from linear-response theory. The effective coupling strength for a connection from neuron j with rate ν_j to neuron i with rate ν_i is defined as [89, Eqs. A.2 and A.3 (correcting a typo in this previous work)]:

$$
\begin{aligned}
w_{ij}^{\mathrm{ecs}} &= \frac{\partial \nu_i}{\partial \nu_j} \\
&= \widetilde{\alpha} J_{ij} + \widetilde{\beta} J_{ij}^2 \\
\text{with} \quad \widetilde{\alpha} &= \sqrt{\pi} \left(\tau_{\mathrm{m}} \nu_i\right)^2 \frac{1}{\sigma_i} \left(f\left(y_\theta\right) - f\left(y_{\mathrm{r}}\right)\right) \\
\text{and} \quad \widetilde{\beta} &= \sqrt{\pi} \left(\tau_{\mathrm{m}} \nu_i\right)^2 \frac{1}{2\sigma_i^2} \left(f\left(y_\theta\right) y_\theta - f\left(y_{\mathrm{r}}\right) y_{\mathrm{r}}\right),
\end{aligned}
\tag{54}
$$

where f and $y_{\{\theta,r\}}$ are defined as in Eq 50. The dashed line in Fig 6B is given by the term $\propto \widetilde{\alpha}$ alone since we also ignore the small contribution of the variance to the transfer function of the LIF neuron [94] .

4.5.2 Linear interpolation

To compute the derivative $d\lambda/d\alpha$ given in Eq 29, we use a method for computing the derivative of an implicit function: If $R\left(\alpha, \lambda\right) = 0$, it follows that the derivative

$$
\frac{d\lambda}{d\alpha} = -\frac{\partial R/\partial \alpha}{\partial R/\partial \lambda} =: -\frac{R_\alpha}{R_\lambda}. \tag{55}
$$

With the characteristic equation for the effective transfer function Eq 27, we get

$$
R\left(\alpha, \lambda\right) = \widetilde{H}_\alpha\left(\lambda\right) \cdot \mathrm{e}^{-\lambda d} \cdot \widehat{p}\left(k\right) - 1 = 0. \tag{56}
$$

The partial derivatives of R with respect to α and λ are

$$
\begin{aligned}
R_\alpha &= \mathrm{e}^{-\lambda d} \cdot \widehat{p}\left(k\right) \cdot \frac{\partial \widetilde{H}_\alpha\left(\lambda\right)}{\partial \alpha} \\
&= \mathrm{e}^{-\lambda d} \cdot \widehat{p}\left(k\right) \cdot \left[\widetilde{H}^{\mathrm{s}}\left(\lambda\right) - \widetilde{H}^{\mathrm{nf}}\left(\lambda\right)\right],
\end{aligned}
$$

and

$$
\begin{aligned}
R_\lambda &= \widehat{p}\left(k\right) \cdot \frac{\partial}{\partial \lambda} \left[\widetilde{H}_\alpha\left(\lambda\right) \cdot \mathrm{e}^{-\lambda d}\right] \\
&= \mathrm{e}^{-\lambda d} \cdot \widehat{p}\left(k\right) \cdot \left[\frac{\partial \widetilde{H}_\alpha\left(\lambda\right)}{\partial \lambda} - d \cdot \widetilde{H}_\alpha\left(\lambda\right)\right] \\
&= \mathrm{e}^{-\lambda d} \cdot \widehat{p}\left(k\right) \cdot \left[\alpha \frac{\partial \widetilde{H}^{\mathrm{s}}\left(\lambda\right)}{\partial \lambda} + \left(1-\alpha\right) \frac{\partial \widetilde{H}^{\mathrm{nf}}\left(\lambda\right)}{\partial \lambda} - d \cdot \widetilde{H}_\alpha\left(\lambda\right)\right] \\
&= \mathrm{e}^{-\lambda d} \cdot \widehat{p}\left(k\right) \cdot \left[\alpha \widetilde{H}_\lambda^{\mathrm{s}}\left(\lambda\right) + \left(1-\alpha\right) \cdot \widetilde{H}_\lambda^{\mathrm{nf}}\left(\lambda\right) - d \cdot \widetilde{H}_\alpha\left(\lambda\right)\right].
\end{aligned}
\tag{57}
$$

4.6 Fixing the working point

For the spiking model, we fix the mean input μ and its variance σ relative to their spiking threshold for both populations. Each neuron receives external excitatory and inhibitory input with Poisson-distributed interspike interval statistics (analogous to [89, Eq. E.1]). The external input rates for excitatory neurons $\nu_{\mathrm{E,ext}}$ and for inhibitory neurons $\nu_{\mathrm{I,ext}}$ are

$$
\nu_{\mathrm{E,ext}} = \nu_{\mathrm{E},0} + \nu_{\mathrm{bal}}, \quad \nu_{\mathrm{I,ext}} = \nu_{\mathrm{bal}}/g, \tag{58}
$$

$$\text{with} \quad \nu_{\mathrm{E},0} = \frac{\mu - \mu_{\mathrm{loc}}}{J_{\mathrm{E}} \tau_{\mathrm{m}}} \qquad \text{and} \quad \nu_{\mathrm{bal}} = \frac{\sigma^2 - \sigma^2_{\mathrm{loc}} - \tau_{\mathrm{m}} \nu_{\mathrm{E},0} J_{\mathrm{E}}^2}{\tau_{\mathrm{m}} J_{\mathrm{E}}^2 (1+g^2)}, \tag{59}$$

where $\mu_{\mathrm{loc}} = \tau_{\mathrm{m}} \nu \, KJ \, (1 - \gamma g)$ and $\sigma^2_{\mathrm{loc}} = \tau_{\mathrm{m}} \nu \, KJ^2 \, \left(1 + \gamma g^2\right)$ are the mean and variance due to local input from other neurons firing with the target rate ν, respectively. The rate ν_{bal} establishes a balance between excitation and inhibition, taking into account the variances, and the rate $\nu_{\mathrm{E},0}$ only applies to the excitatory neurons with the aim to shift the mean.

4.7 Physical units

The sub-threshold dynamics of the LIF neuron in Eq 13 are, without loss of generality, given in scaled units. In this formulation, V, J and I are all quantities with unit Volt. For the parameter-wise comparison with numerical network simulation (for example using NEST [98]), it is useful to consider a description where $I^{'}$ and $J^{'}$ represent electric currents in units of Ampere:

$$\begin{aligned} \tau_{\mathrm{m}} \frac{dV_i^{'}}{dt} &= -\left(V_i^{'} - E_{\mathrm{L}}\right) + R_{\mathrm{m}} I_i^{'}(t) \\ \tau_{\mathrm{s}} \frac{dI_i^{'}}{dt} &= -I_i^{'} + \tau_{\mathrm{s}} \sum_j J_{ij}^{'} s_j \left(t - d\right). \end{aligned} \tag{60}$$

Here, we also introduce a resistive leak reversal potential E_{L}, and shift threshold and reset potentials $V_\theta' = V_\theta + E_{\mathrm{L}}$ and $V_r' = V_r + E_{\mathrm{L}}$, respectively. The membrane time constant $\tau_{\mathrm{m}} = R_{\mathrm{m}} C_{\mathrm{m}}$ relates the membrane resistance R_{m} and capacitance C_{m}. In units of Ampere, the total current input $I^{'} = I/R_{\mathrm{m}}$ and the synaptic weight amplitude $J^{'} = C_{\mathrm{m}} J/\tau_{\mathrm{s}}$.

4.8 Network structure and parameters

We simulate recurrently connected neural networks of one excitatory and one inhibitory populations each using the neural simulation software NEST [111], using either spiking- or rate-neuron models. The support for rate neurons in NEST was recently added as described in [97]. Figs 10 and 11 provide the complete neuron and network model descriptions and Fig 12 summarizes all parameters as used for the network state showing periodic traveling waves (marked by black star in Fig 1D, Fig 5D and Fig 8C). Other simulation parameters used to obtain other network states shown throughout this paper are indicated with a ⊛ marker in Fig 12, and the changed parameters are given in the corresponding figures. The same marker always denotes the same parameter combination across figure panels. The tables distinguish between network properties and parameters valid for both spiking and rate neuron models and those specific to only one neuron model. Irrespective of the choice of neuron model (rate vs. spiking), the neuron parameters are shared between both neuron populations. The neurons of each population are positioned with equal spacing along a one-dimensional path of perimeter L and connections between neurons are drawn according to a distance-dependent rule with periodic boundary conditions (a "ring" network) using the NEST Topology module.

The number of excitatory neurons N_{E} in our network is four times larger than the number of inhibitory neurons N_{I} [112]. The number of incoming connections, the in-degree $K_{\{\mathrm{E,I}\}}$, is proportional to the population size of the presynaptic population, assuming an overall connection probability of 10%. Around each postsynaptic neuron, the connection algorithm establishes connections from neighboring neurons within a

Model summary	
Populations	Excitatory (E), inhibitory (I)
Topology	Ring network: Neurons positioned equally spaced on one-dimensional domain of length L; periodic boundary conditions
Connectivity	Random convergent connections with fixed in-degree, distance-dependent boxcar-shaped spatial profiles realized with cut-off masks
Spiking model	
Neuron model	Leaky integrate-and-fire (LIF), fixed threshold, absolute refractory time
Synapse model	Static weights and delays, exponentially shaped postsynaptic currents
Input	Independent fixed-rate Poisson spike trains to all neurons (excitatory and inhibitory Poisson sources)
Measurement	Spike activity
Rate model	
Neuron model	Rate neuron with tanh gain function
Synapse model	Delayed rate connection
Input	-
Measurement	Activity

Figure 10. Summary of network models following the guidelines of Nordlie et al. [110]. Separation between nonlinear spiking and rate neurons as used in NEST simulations.

distance of $R_{\{\mathrm{E,I}\}}$. The width of the profile depends on the presynaptic population alone. Potentially presynaptic neurons within this distance are picked at random and connections are established until the fixed in-degree is reached. Multiple connections between the same pair of neurons termed multapses are allowed, but self-connections (autapses) are prohibited.

The leaky integrate-and-fire model with exponential postsynaptic currents is implemented in NEST under the name `iaf_psc_exp`. The neuron parameters are the same as in the microcircuit model of [113] with the difference that our membrane time constant τ_{m} is half of theirs and that we here omit the refractory period τ_{ref}, although our results generalize to a non-zero τ_{ref}. An excitatory and an inhibitory Poisson generator provide external input to all neurons. Their rates $\nu_{\{\mathrm{E,I}\},\mathrm{ext}}$ are determined according to Eq 58 for fixing the working point (μ, σ).

The dynamics of rate-based units in NEST is specified as stochastic differential equations using the Itô convention [97], except that we here set the stochasticity (the variance of the input) to zero. We use the neuron model `tanh_ipn`, that employs a hyperbolic tangent as a gain function.

Simulations run for a simulation time T_{sim} with a temporal resolution of dt. During rate simulations, the instantaneous rate is recorded once at each time step dt. Our raster plots from simulations of the spiking model and the image plots from simulation of the rate model show the network activity from all simulated neurons after a start-up transient T_{trans}.

4.9 Software and implementation

Spiking- and rate-neuron network simulations were implemented in NEST v2.14.0 [98], and Python v2.7.11. Post-processing and plotting relied on Python with numpy v1.10.4, SciPy v0.17.0, and matplotlib v2.0.2.

Network models	
Distance-dependent connectivity	Neural units $j \in X$ at location x_j and $i \in Y$ at x_i in pre- and postsynaptic populations X and Y, respectively. Displacement between units i and j: $r_{ij} = x_i - x_j$ Boxcar-shaped spatial profile with width R and Heaviside function Θ: $p(r_{ij}) = \frac{1}{2R}\Theta(R - \lvert r_{ij}\rvert)$
Spiking model	
Subthreshold dynamics	If $t > t^* + \tau_{\text{ref}}$ $\frac{\mathrm{d}V}{\mathrm{d}t} = -\frac{V - E_{\text{L}}}{\tau_{\text{m}}} + \frac{I_{\text{syn}}(t)}{C_{\text{m}}}$ $I_{\text{syn}}(t) = \sum_j J_j I_{\text{PSC}}\left(t - t_j^* - d\right)$ with connection strength J_j, presynaptic spike time t_j^* and conduction delay d $I_{\text{PSC}}(t) = \mathrm{e}^{t/\tau_{\text{s}}}\Theta(t)$ with Heaviside function Θ else $V(t) = V_r$
Spiking	If $V(t-) < V_\theta \wedge V(t+) \geq V_\theta$ 1. set $t^* = t$ 2. emit spike with timestamp t^* 3. reset $V(t) = V_{\text{r}}$
Rate model	
Differential equation	$\tau\frac{\mathrm{d}u}{\mathrm{d}t} = -u(t) + \sum_{j=1} w_j \psi(u_j(t-d))$ $\psi(x) = \tanh(x)$

Figure 11. Description of network models. Separation between nonlinear spiking and rate neurons as used in NEST simulations.

A: Global simulation parameters		
Symbol	**Value**	**Description**
T_{sim}	350 ms	Simulation duration
T_{trans}	150 ms	Start-up transient
dt	0.1 ms	Temporal resolution
B: Populations and external input		
Symbol	**Value**	**Description**
N_{E}	4,000	Population size of excitatory neurons
N_{I}	1,000	Population size of inhibitory neurons
L	1 mm	Domain length
		Spiking model
μ	10 mV	Mean input relative to firing threshold
σ	10 mV	Variance of input relative to firing threshold
$\nu_{\mathrm{E,ext}}$	35085 Hz	⊛ Excitatory external rate (by fixing working point)
$\nu_{\mathrm{I,ext}}$	3683 Hz	⊛ Inhibitory external rate (by fixing working point)
C: Connection parameters		
Symbol	**Value**	**Description**
R_{E}	0.2 mm	⊛ Profile width of excitatory neurons
R_{I}	0.07 mm	⊛ Profile width of inhibitory neurons
d	3 ms	⊛ Delay
		Spiking model
K_{E}	400	In-degree from excitatory neurons
γ	0.25	Relative in-degree, $\gamma = K_{\mathrm{I}}/K_{\mathrm{E}}$
J'_{E}	87.8 pA	⊛ Reference synaptic strength
g	5	⊛ Relative synaptic strength, $g = -J_{\mathrm{I}}/J_{\mathrm{E}}$
		Rate model
w_{E}	2.73	⊛ Excitatory weight (by parameter mapping)
w_{I}	−3.42	⊛ Inhibitory weight (by parameter mapping)
D: Neuron model		
Symbol	**Value**	**Description**
		Spiking model
C_{m}	250 pF	Membrane capacitance
τ_{m}	5 ms	Membrane time constant
E_{L}	−65 mV	Resting potential
V_θ	−50 mV	Firing threshold
V_{r}	−65 mV	Reset potential
τ_{ref}	0 ms	Absolute refractory period
τ_{s}	0.5 ms	Postsynaptic current time constant
		Rate model
τ	1.94 ms	Time constant (by parameter mapping)

Figure 12. Simulation and network parameters. Parameters according to setting for traveling waves as shown in Fig 1D, Fig 5D and Fig 8C (black star marker). Deviant parameters are given in the captions of the respective figures and indicated by different markers.

Acknowledgments

The authors would like to thank the whole INM-6 for fruitful discussions; in particular Michael Denker and Sonja Grün for sharing their experience on wave-like activity in experimentally recorded brain activity, and David Dahmen, Hannah Bos and other colleagues from the NEST community (http://www.nest-simulator.org).

Funding

This project has received funding from the Helmholtz association: portfolio Supercomputing and Modeling for the Human Brain (SMHB), young investigator group VH-NG-1028; the European Union's Horizon 2020 research and innovation programme under grant agreement No 720270 (HBP SGA1), the German Research Foundation (DFG; grant DI 1721/3-1 [KFO219-TP9]), the ERS grant "Facing the multi-scale problem in neuroscience" of the RWTH Aachen University, and the Research Council of Norway (NFR through COBRA). The funders had no role in study design, data collection and analysis, decision to publish, or preparation of the manuscript.

References

1. Rubino D, Robbins KA, Hatsopoulos NG. Propagating waves mediate information transfer in the motor cortex. Nat Neurosci. 2006;9(12):1549–1557. doi:10.1038/nn1802.
2. Nauhaus I, Busse L, Carandini M, Ringach DL. Stimulus contrast modulates functional connectivity in visual cortex. Nat Neurosci. 2009;12(1):70–76. doi:10.1038/nn.2232.
3. Muller L, Destexhe A. Propagating waves in thalamus, cortex and the thalamocortical system: experiments and models. J Physiol Paris. 2012;106(5–6):222–238. doi:10.1016/j.jphysparis.2012.06.005.
4. Sato TK, Nauhaus I, Carandini M. Traveling Waves in Visual Cortex. Neuron. 2012;75(2):218–229. doi:10.1016/j.neuron.2012.06.029.
5. Muller L, Reynaud A, Chavane F, Destexhe A. The stimulus-evoked population response in visual cortex of awake monkey is a propagating wave. Nat Commun. 2014;5:3675. doi:10.1038/ncomms4675.
6. Townsend RG, Solomon SS, Chen SC, Pietersen ANJ, Martin PR, Solomon SG, et al. Emergence of Complex Wave Patterns in Primate Cerebral Cortex. J Neurosci. 2015;35(11):4657–4662. doi:10.1523/jneurosci.4509-14.2015.
7. Zanos TP, Mineault PJ, Nasiotis KT, Guitton D, Pack CC. A Sensorimotor Role for Traveling Waves in Primate Visual Cortex. Neuron. 2015;85(3):615–627. doi:10.1016/j.neuron.2014.12.043.
8. Denker M, Zehl L, Kilavik BE, Diesmann M, Brochier T, Riehle A, et al. LFP beta amplitude is predictive of mesoscopic spatio-temporal phase patterns. arXiv preprint arXiv:170309488. 2017;.
9. Kim U, Bal T, McCormick DA. Spindle waves are propagating synchronized oscillations in the ferret LGNd in vitro. J Neurophysiol. 1995;74(3):1301–1323. doi:10.1152/jn.1995.74.3.1301.

10. Lubenov EV, Siapas AG. Hippocampal theta oscillations are travelling waves. Nature. 2009;459(7246):534–539. doi:10.1038/nature08010.

11. Riehle A, Wirtssohn S, Grün S, Brochier T. Mapping the spatio-temporal structure of motor cortical LFP and spiking activities during reach-to-grasp movements. Front Neural Circuit. 2013;7:48. doi:10.3389/fncir.2013.00048.

12. Takahashi K, Kim S, Coleman TP, Brown KA, Suminski AJ, Best MD, et al. Large-scale spatiotemporal spike patterning consistent with wave propagation in motor cortex. Nat Commun. 2015;6:7169. doi:10.1038/ncomms8169.

13. Ferezou I, Bolea S, Petersen CC. Visualizing the cortical representation of whisker touch: voltage-sensitive dye imaging in freely moving mice. Neuron. 2006;50(4):617–629. doi:10.1016/j.neuron.2006.03.043.

14. Garaschuk O, Linn J, Eilers J, Konnerth A. Large-scale oscillatory calcium waves in the immature cortex. Nat Neurosci. 2000;3(5):452–459. doi:10.1038/74823.

15. Mehring C, Hehl U, Kubo M, Diesmann M, Aertsen A. Activity dynamics and propagation of synchronous spiking in locally connected random networks. Biol Cybern. 2003;88(5):395–408. doi:10.1007/s00422-002-0384-4.

16. Yger P, Boustani SE, Destexhe A, Frégnac Y. Topologically invariant macroscopic statistics in balanced networks of conductance-based integrate-and-fire neurons. J Comput Neurosci. 2011;31(2):229–245. doi:10.1007/s10827-010-0310-z.

17. Voges N, Perrinet L. Complex dynamics in recurrent cortical networks based on spatially realistic connectivities. Front Comput Neurosc. 2012;6. doi:10.3389/fncom.2012.00041.

18. Keane A, Gong P. Propagating Waves Can Explain Irregular Neural Dynamics. J Neurosci. 2015;35(4):1591–1605. doi:10.1523/jneurosci.1669-14.2015.

19. Voges N, Schüz A, Aertsen A, Rotter S. A modeler's view on the spatial structure of intrinsic horizontal connectivity in the neocortex. Prog Neurobiol. 2010;92(3):277–292. doi:10.1016/j.pneurobio.2010.05.001.

20. Hellwig B. A quantitative analysis of the local connectivity between pyramidal neurons in layers 2/3 of the rat visual cortex. Biol Cybern. 2000;82(2):111–121. doi:10.1007/PL00007964.

21. Perin R, Berger TK, Markram H. A synaptic organizing principle for cortical neuronal groups. P Natl A Sci. 2011;108(13):5419–5424. doi:10.1073/pnas.1016051108.

22. Schnepel P, Kumar A, Zohar M, Aertsen A, Boucsein C. Physiology and Impact of Horizontal Connections in Rat Neocortex. Cereb Cortex. 2015;25(10):3818–3835. doi:10.1093/cercor/bhu265.

23. Wilson HR, Cowan JD. Excitatory and Inhibitory Interactions in Localized Populations of Model Neurons. Biophys J. 1972;12(1):1–24. doi:10.1016/s0006-3495(72)86068-5.

24. Wilson HR, Cowan JD. A mathematical theory of the functional dynamics of cortical and thalamic nervous tissue. Kybernetik. 1973;13(2):55–80. doi:10.1007/bf00288786.

25. Amari S. Dynamics of pattern formation in lateral-inhibition type neural fields. Biol Cybern. 1977;27(2):77–87. doi:10.1007/bf00337259.

26. Erlhagen W. Lokalisierte, stationäre Verteilung in neuronalen Feldern: Modellierung experimenteller Befunde zur Planung und Kontrolle zielgerichteter Bewegungen. Thun, Frankfurt/Main: Verlag Harri Deutsch; 1997.

27. Bressloff PC, Carroll SR. Laminar neural field model of laterally propagating waves of orientation selectivity. PLOS Comput Biol. 2015;11(10):1–26. doi:10.1371/journal.pcbi.1004545.

28. Ermentrout B. Neural networks as spatio-temporal pattern-forming systems. Rep Prog Phys. 1998;61(4):353. doi:10.1088/0034-4885/61/4/002.

29. Coombes S. Waves, bumps, and patterns in neural field theories. Biol Cybern. 2005;93(2):91–108. doi:10.1007/s00422-005-0574-y.

30. Wyller J, Blomquist P, Einevoll GT. On the origin and properties of two-population neural field models - a tutorial introduction. Biophys Rev Lett. 2007;2(01):79–98. doi:10.1142/s1793048007000441.

31. Coombes S. Large-scale neural dynamics: simple and complex. NeuroImage. 2010;52(3):731–739. doi:10.1016/j.neuroimage.2010.01.045.

32. Bressloff PC. Spatiotemporal dynamics of continuum neural fields. J Phys A-Math Theor. 2012;45(3):033001. doi:10.1088/1751-8113/45/3/033001.

33. Bressloff PC. Waves in neural media. Lecture notes on mathematical modelling in the life sciences ed. Springer; 2014. Available from: `https://link.springer.com/book/10.1007%2F978-1-4614-8866-8`.

34. Coombes S, beim Graben P, Potthast R, Wright J, editors. Neural Fields: Theory and Applications. Springer; 2014. Available from: `http://www.springer.com/de/book/9783642545924`.

35. Ermentrout G, Cowan JD. Temporal oscillations in neuronal nets. J Math Biol. 1979;7(3):265–280. doi:10.1007/bf00275728.

36. Ermentrout GB, Cowan JD. A mathematical theory of visual hallucination patterns. Biol Cybern. 1979;34(3):137–150. doi:10.1007/bf00336965.

37. Ermentrout GB, Cowan J. Large scale spatially organized activity in neural nets. SIAM J Appl Math. 1980;38(1):1–21. doi:10.1137/0138001.

38. Ermentrout G, Cowan J. Secondary bifurcation in neuronal nets. SIAM J Appl Math. 1980;39(2):323–340. doi:10.1137/0139028.

39. Bressloff PC. New Mechanism for Neural Pattern Formation. Phys Rev Lett. 1996;76(24):4644–4647. doi:10.1103/PhysRevLett.76.4644.

40. Hutt A, Bestehorn M, Wennekers T. Pattern formation in intracortical neuronal fields. Network. 2003;14(2):351–368. doi:10.1088/0954-898X_14_2_310.

41. Bressloff PC, Kilpatrick ZP. Nonlocal Ginzburg-Landau equation for cortical pattern formation. Phys Rev E. 2008;78(4):041916. doi:10.1103/PhysRevE.78.041916.

42. Roxin A, Brunel N, Hansel D. Role of Delays in Shaping Spatiotemporal Dynamics of Neuronal Activity in Large Networks. Phys Rev Lett. 2005;94(23):238103. doi:10.1103/PhysRevLett.94.238103.

43. Atay FM, Hutt A. Neural fields with distributed transmission speeds and long-range feedback delays. SIAM J Appl Dyn Syst. 2006;5(4):670–698. doi:10.1137/050629367.

44. Venkov NA, Coombes S, Matthews PC. Dynamic instabilities in scalar neural field equations with space-dependent delays. Physica D. 2007;232(1):1–15. doi:10.1016/j.physd.2007.04.011.

45. Coombes S, Venkov NA, Shiau L, Bojak I, Liley DTJ, Laing CR. Modeling electrocortical activity through improved local approximations of integral neural field equations. Phys Rev E. 2007;76(5):051901. doi:10.1103/PhysRevE.76.051901.

46. Turing AM. The chemical basis of morphogenesis. Philos T R Soc B. 1952;237(641):37–72. doi:10.1098/rstb.1952.0012.

47. Kuramoto Y. Chemical oscillations, waves, and turbulence. Springer-Verlag Berlin Heidelberg New York Tokyo; 1984. Available from: `https://link.springer.com/book/10.1007%2F978-3-642-69689-3`.

48. Hutt A, Atay FM. Analysis of nonlocal neural fields for both general and gamma-distributed connectivities. Physica D. 2005;203(1):30–54. doi:10.1016/j.physd.2005.03.002.

49. Wyller J, Blomquist P, Einevoll GT. Turing instability and pattern formation in a two-population neuronal network model. Physica D. 2007;225(1):75–93. doi:10.1016/j.physd.2006.10.004.

50. Folias S, Ermentrout G. Bifurcations of Stationary Solutions in an Interacting Pair of E-I Neural Fields. SIAM J Appl Dyn Syst. 2012;11(3):895–938. doi:10.1137/110860094.

51. Roxin A, Brunel N, Hansel D. Rate Models with Delays and the Dynamics of Large Networks of Spiking Neurons. Prog Theor Phys Supp. 2006;161:68–85. doi:10.1143/PTPS.161.68.

52. Jirsa VK, Kelso JAS. Spatiotemporal pattern formation in neural systems with heterogeneous connection topologies. Phys Rev E. 2000;62(6):8462–8465. doi:10.1103/PhysRevE.62.8462.

53. Atay F, Hutt A. Stability and Bifurcations in Neural Fields with Finite Propagation Speed and General Connectivity. SIAM J Appl Math. 2005;65(2):644–666. doi:10.1137/S0036139903430884.

54. Hutt A. Local excitation-lateral inhibition interaction yields oscillatory instabilities in nonlocally interacting systems involving finite propagation delay. Phys Lett A. 2008;372(5):541–546. doi:10.1016/j.physleta.2007.08.018.

55. Bojak I, Liley DTJ. Axonal Velocity Distributions in Neural Field Equations. PLOS Comput Biol. 2010;6(1):1–25. doi:10.1371/journal.pcbi.1000653.

56. Hutt A, Rougier N. Activity spread and breathers induced by finite transmission speeds in two-dimensional neural fields. Phys Rev E. 2010;82(5):055701. doi:10.1103/PhysRevE.82.055701.

57. Veltz R. An analytical method for computing Hopf bifurcation curves in neural field networks with space-dependent delays. C R Math. 2011;349(13):749–752. doi:10.1016/j.crma.2011.06.014.

58. Veltz R. Interplay Between Synaptic Delays and Propagation Delays in Neural Field Equations. SIAM J Appl Dyn Syst. 2013;12(3):1566–1612. doi:10.1137/120889253.

59. Softky WR, Koch C. The highly irregular firing of cortical cells is inconsistent with temporal integration of random EPSPs. J Neurosci. 1993;13(1):334–350.

60. Brunel N, Hakim V. Fast Global Oscillations in Networks of Integrate-and-Fire Neurons with Low Firing Rates. Neural Comput. 1999;11(7):1621–1671. doi:10.1162/089976699300016179.

61. Ecker AS, Berens P, Keliris GA, Bethge M, Logothetis NK, Tolias AS. Decorrelated neuronal firing in cortical microcircuits. Science. 2010;327(5965):584–587. doi:10.1126/science.1179867.

62. Hutt A, Hashemi M, Graben Pb. How to Render Neural Fields More Realistic. In: Validating Neuro-Computational Models of Neurological and Psychiatric Disorders. Springer Series in Computational Neuroscience. Springer, Cham; 2015. p. 141–159. Available from: `https://link.springer.com/chapter/10.1007/978-3-319-20037-8_6`.

63. Montbrió E, Pazó D, Roxin A. Macroscopic Description for Networks of Spiking Neurons. Phys Rev X. 2015;5(2):021028. doi:10.1103/PhysRevX.5.021028.

64. Amit DJ, Brunel N. Dynamics of a recurrent network of spiking neurons before and following learning. Network. 1997;8(4):373–404. doi:10.1088/0954-898X_8_4_003.

65. Brunel N. Dynamics of Sparsely Connected Networks of Excitatory and Inhibitory Spiking Neurons. J Comput Neurosci. 2000;8(3):183–208. doi:10.1023/a:1008925309027.

66. Lindner B, Doiron B, Longtin A. Theory of oscillatory firing induced by spatially correlated noise and delayed inhibitory feedback. Phys Rev E. 2005;72(6):061919. doi:10.1103/PhysRevE.72.061919.

67. Golomb D, Ermentrout GB. Bistability in Pulse Propagation in Networks of Excitatory and Inhibitory Populations. Phys Rev Lett. 2001;86(18):4179–4182. doi:10.1103/PhysRevLett.86.4179.

68. Cremers D, Herz AVM. Traveling Waves of Excitation in Neural Field Models: Equivalence of Rate Descriptions and Integrate-and-Fire Dynamics. Neural Comput. 2002;14(7):1651–1667. doi:10.1162/08997660260028656.

69. Osan R, Ermentrout B. The evolution of synaptically generated waves in one- and two-dimensional domains. Physica D. 2002;163(3):217–235. doi:10.1016/S0167-2789(02)00347-0.

70. Fohlmeister C, Gerstner W, Ritz R, Hemmen JLv. Spontaneous Excitations in the Visual Cortex: Stripes, Spirals, Rings, and Collective Bursts. Neural Comput. 1995;7(5):905–914. doi:10.1162/neco.1995.7.5.905.

71. Kistler WM, Seitz R, van Hemmen JL. Modeling collective excitations in cortical tissue. Physica D. 1998;114(3):273–295. doi:10.1016/S0167-2789(97)00195-4.

72. Kistler WM. Stability properties of solitary waves and periodic wave trains in a two-dimensional network of spiking neurons. Phys Rev E. 2000;62(6):8834–8837. doi:10.1103/PhysRevE.62.8834.

73. Bressloff PC. Traveling waves and pulses in a one-dimensional network of excitable integrate-and-fire neurons. J Math Biol. 2000;40(2):169–198. doi:10.1007/s002850050008.

74. Crook SM, Ermentrout GB, Vanier MC, Bower JM. The Role of Axonal Delay in the Synchronization of Networks of Coupled Cortical Oscillators. J Comput Neurosci. 1997;4(2):161–172. doi:10.1023/A:1008843412952.

75. Ermentrout B. Reduction of Conductance-Based Models with Slow Synapses to Neural Nets. Neural Comput. 1994;6(4):679–695. doi:10.1162/neco.1994.6.4.679.

76. Bressloff PC, Coombes S. Spike Train Dynamics Underlying Pattern Formation in Integrate-and-Fire Oscillator Networks. Phys Rev Lett. 1998;81(11):2384–2387. doi:10.1103/PhysRevLett.81.2384.

77. Bressloff P, Coombes S. A Dynamical Theory of Spike Train Transitions in Networks of Integrate-and-Fire Oscillators. SIAM J Appl Math. 2000;60(3):820–841. doi:10.1137/S0036139998339643.

78. Haken H. Quasi-discreted dynamics of a neural net: The lighthouse model. Discrete Dyn Nat Soc. 2000;4(3):187–200. doi:10.1155/S1026022600000182.

79. Haken H. Phase Locking in the Lighthouse Model of a Neural Net with Several Delay Times. Prog Theor Phys Supp. 2000;139:96–111. doi:10.1143/PTPS.139.96.

80. Chow C, Coombes S. Existence and Wandering of Bumps in a Spiking Neural Network Model. SIAM J Appl Dyn Syst. 2006;5(4):552–574. doi:10.1137/060654347.

81. Laing CR, Chow CC. Stationary Bumps in Networks of Spiking Neurons. Neural Comput. 2001;13(7):1473–1494. doi:10.1162/089976601750264974.

82. Rosenbaum R, Doiron B. Balanced Networks of Spiking Neurons with Spatially Dependent Recurrent Connections. Phys Rev X. 2014;4(2):021039. doi:10.1103/physrevx.4.021039.

83. Rosenbaum R, Smith MA, Kohn A, Rubin JE, Doiron B. The spatial structure of correlated neuronal variability. Nat Neurosci. 2016;20(1):107–114. doi:10.1038/nn.4433.

84. Pyle R, Rosenbaum R. Spatiotemporal Dynamics and Reliable Computations in Recurrent Spiking Neural Networks. Phys Rev Lett. 2017;118(1):018103. doi:10.1103/PhysRevLett.118.018103.

85. Kriener B, Helias M, Rotter S, Diesmann M, Einevoll GT. How pattern formation in ring networks of excitatory and inhibitory spiking neurons depends on the input current regime. Front Comput Neurosc. 2014;7. doi:10.3389/fncom.2013.00187.

86. Senk J, Korvasová K, Schuecker J, Hagen E, Tetzlaff T, Diesmann M, et al. Conditions for traveling waves in spiking neural networks obtained from a rigorous mapping to a neural-field model. In: 26th Annual Computational Neuroscience Meeting (CNS*2017), BMC Neuroscience 2017, 18(Suppl 1):P94; 2017.Available from: http://dx.doi.org/10.1186/s12868-017-0371-2.

87. Corless RM, Gonnet GH, Hare DEG, Jeffrey DJ, Knuth DE. On the LambertW function. Advances in Computational Mathematics. 1996;5(1):329–359. doi:10.1007/BF02124750.

88. van Vreeswijk C, Sompolinsky H. Chaos in Neuronal Networks with Balanced Excitatory and Inhibitory Activity. Science. 1996;274(5293):1724–1726. doi:10.1126/science.274.5293.1724.

89. Helias M, Tetzlaff T, Diesmann M. Echoes in correlated neural systems. New J Phys. 2013;15(2):023002. doi:10.1088/1367-2630/15/2/023002.

90. Fourcaud-Trocmé N, Brunel N. Dynamics of the Instantaneous Firing Rate in Response to Changes in Input Statistics. J Comput Neurosci. 2005;18(3):311–321. doi:10.1007/s10827-005-0337-8.

91. Tuckwell HC. Introduction to Theoretical Neurobiology. vol. 2. Cambridge University Press; 1988. Available from: https://www.cambridge.org/core/books/introduction-to-theoretical-neurobiology/5B00C4410746818CE64451F201CD1FE7.

92. Ricciardi L, Crescenzo A, Giorno V, Nobile A. An outline of theoretical and algorithmic approaches to first passage time problems with applications to biological modeling. Math Japon. 1999;50(2):247–322.

93. Risken H. Fokker-planck equation. In: The Fokker-Planck Equation. Springer; 1996. p. 63–95. Available from: http://dx.doi.org/10.1007/978-3-642-61544-3_4.

94. Schuecker J, Diesmann M, Helias M. Modulated escape from a metastable state driven by colored noise. Phys Rev E. 2015;92(5):052119. doi:10.1103/physreve.92.052119.

95. Lindner B, Schimansky-Geier L. Transmission of Noise Coded versus Additive Signals through a Neuronal Ensemble. Phys Rev Lett. 2001;86(14):2934–2937. doi:10.1103/PhysRevLett.86.2934.

96. Brunel N, Chance FS, Fourcaud N, Abbott LF. Effects of Synaptic Noise and Filtering on the Frequency Response of Spiking Neurons. Phys Rev Lett. 2001;86(10):2186–2189. doi:10.1103/PhysRevLett.86.2186.

97. Hahne J, Dahmen D, Schuecker J, Frommer A, Bolten M, Helias M, et al. Integration of continuous-time dynamics in a spiking neural network simulator. Front Neuroinform. 2017;11:34. doi:10.3389/fninf.2017.00034.

98. Peyser A, Sinha A, Vennemo SB, Ippen T, Jordan J, Graber S, et al.. NEST 2.14.0; 2017. Available from: http://dx.doi.org/10.5281/zenodo.882970.

99. Eccles JC, Fatt P, Koketsu K. Cholinergic and inhibitory synapses in a pathway from motor-axon collaterals to motoneurones. The Journal of physiology. 1954;126(3):524–562. doi:10.1113/jphysiol.1954.sp005226.

100. Stepanyants A, Martinez LM, Ferecskó AS, Kisvárday ZF. The fractions of short-and long-range connections in the visual cortex. Proc Natl Acad Sci USA. 2009;106(9):3555–3560. doi:10.1073/pnas.0810390106.

101. Cross MC, Hohenberg PC. Pattern formation outside of equilibrium. Rev Mod Phys. 1993;65(3):851–1112. doi:10.1103/RevModPhys.65.851.

102. Legenstein R, Maass W. Edge of chaos and prediction of computational performance for neural circuit models. Neural Netw. 2007;20(3):323–334. doi:10.1016/j.neunet.2007.04.017.

103. Fermani F, Richardson MJ. Coarse-grained description of the spatio-temporal dynamics of network activity from experimentally verified single-neuron models and connectivity. In: 24th Annual Computational Neuroscience Meeting: CNS*2015, BMC Neuroscience 2015, 16(Suppl 1):P206; 2015.Available from: `http://www.biomedcentral.com/1471-2202/16/S1/P206`.

104. Nordlie E, Tetzlaff T, Einevoll GT. Rate dynamics of leaky integrate-and-fire neurons with strong synapses. Frontiers in computational neuroscience. 2010;4. doi:10.3389/fncom.2010.00149.

105. Heiberg T, Kriener B, Tetzlaff T, Casti A, Einevoll GT, Plesser HE. Firing-rate models capture essential response dynamics of LGN relay cells. J Comput Neurosci. 2013;35(3):359–375. doi:10.1007/s10827-013-0456-6.

106. Casti A, Hayot F, Xiao Y, Kaplan E. A simple model of retina-LGN transmission. J Comput Neurosci. 2008;24(2):235–252. doi:10.1007/s10827-007-0053-7.

107. Gerstner W. Population dynamics of spiking neurons: fast transients, asynchronous states, and locking. Neural Comput. 2000;12(1):43–89. doi:10.1162/089976600300015899.

108. Fourcaud N, Brunel N. Dynamics of the Firing Probability of Noisy Integrate-and-Fire Neurons. Neural Comput. 2002;14(9):2057–2110. doi:10.1162/089976602320264015.

109. Abramowitz M, Stegun IA. Handbook of Mathematical Functions: with Formulas, Graphs, and Mathematical Tables. New York: Dover Publications; 1974. Available from: `http://aapt.scitation.org/doi/10.1119/1.15378`.

110. Nordlie E, Gewaltig MO, Plesser HE. Towards reproducible descriptions of neuronal network models. PLOS Comput Biol. 2009;5(8):e1000456. doi:10.1371/journal.pcbi.1000456.

111. Gewaltig MO, Diesmann M. NEST (NEural Simulation Tool). Scholarpedia. 2007;2(4):1430. doi:10.4249/scholarpedia.1430.

112. Braitenberg V. Brain Size and Number of Neurons: An Exercise in Synthetic Neuroanatomy. J Comput Neurosci. 2001;10(1):71–77. doi:10.1023/A:1008920127052.

113. Potjans TC, Diesmann M. The cell-type specific cortical microcircuit: relating structure and activity in a full-scale spiking network model. Cereb cortex. 2014;24(3):785–806. doi:10.1093/cercor/bhs358.